1 Precise age for the Permian-Triassic boundary in South China from
2 high precision U-Pb geochronology and Bayesian age-depth
3 modelling

4 Björn Baresel[1], Hugo Bucher[2], Morgane Brosse[2], Fabrice Cordey[3], Kuang Guodun[4], Urs Schaltegger[1]

5 [1]Department of Earth Sciences, University of Geneva, Geneva, 1205, Switzerland
6 [2]Paleontological Institute and Museum, University of Zurich, Zurich, 8006, Switzerland
7 [3]Laboratoire de Géologie de Lyon, CNRS-UMR 5265, Université Claude Bernard Lyon 1, Villeurbanne, 69622, France
8 [4]Guangxi Bureau of Geology and Mineral Resources, Nanning, 530023, China

9 *Correspondence to*: Björn Baresel (bjorn.baresel@unige.ch)

10 **Abstract.** This study is based on zircon U-Pb ages of 12 volcanic ash layers and volcanogenic sandstones from two marine
11 sections with conformable formational Permian-Triassic boundaries (PTB) in the Nanpanjiang Basin (South China). Our
12 dates of single, thermally annealed and chemically abraded zircons bracket the PTB in Dongpan and Penglaitan and provide
13 the basis for a first proof-of-concept study utilizing a Bayesian chronology model comparing the three sections of Dongpan,
14 Penglaitan and the Global Stratotype Section and Point (GSSP) Meishan. Our Bayesian modeling demonstrates that the
15 formational boundaries in Dongpan (251.938 ± 0.029 Ma), Penglaitan (251.982 ± 0.031 Ma) and Meishan (251.956 ± 0.033
16 Ma) are synchronous within analytical uncertainty of ca. 30 ka. It also provides quantitative evidence that the ages of the
17 paleontologically defined boundaries, based on conodont Unitary Associations zones in Meishan and on macrofaunas in
18 Dongpan, are identical and coincide with the age of the formational boundaries. The age model also confirms the extreme
19 condensation around the PTB in Meishan, which distorts the projection of any stratigraphic points or intervals onto other
20 more expanded sections by means of Bayesian age-depth models. Dongpan and Penglaitan possess significantly higher
21 sedimentation rates and thus offer a greater potential for high resolution studies of environmental proxies and correlations
22 around the PTB than Meishan. This study highlights the power of high-resolution radio-isotopic ages that allow a robust
23 intercalibration of patterns of biotic changes and fluctuating environmental proxies and will help recognizing their global,
24 regional or local significance.

25 1 Introduction

26 The Permian-Triassic boundary mass extinction (PTBME) is considered as the largest mass extinction within the
27 Phanerozoic. About 90 % of all marine species suffered extinction (Raup, 1979; Stanley and Yang, 1994; Erwin et al., 2002;
28 Alroy et al., 2008) and terrestrial plant communities underwent major ecological reorganisation (Hochuli et al., 2010). This
29 major caesura in global biodiversity marked the end of the Palaeozoic faunas and the inception of the modern marine and
30 terrestrial ecosystems (e.g., Benton, 2010; Van Valen, 1984). Several kill mechanisms has been proposed, such as global

31   regression (e.g., Erwin 1990; Yin et al., 2014), marine anoxia (e.g., Feng and Algeo, 2014), ocean acidification (e.g., Payne

32   et al., 2010) or a combination thereof. Rapid global warming (e.g., Svensen et al., 2009), high nutrient fluxes from continent

33   into oceans (Winguth and Winguth, 2012) and increased sedimentation rates (Algeo and Twitchett, 2010) also came into the

34   play, but their respective relations with the global regression near the PTB and the main extinction peak at the PTB remain

35   unclear. In spite of the rapidly growing amount of data, the detailed timing of available diversity estimates and

36   environmental proxies is still lacking, and the ultimate triggers of the PTBME remain elusive. The most likely cause derives

37   from the temporal coincidence with plume-induced massive volcanism of the Siberian Traps (e.g., Burgess and Bowring,

38   2015) that injected excessive amounts of volatiles (H_2O, CO_2, SO_2, H_2S) into the atmosphere. Accompanying

39   destabilization of gas hydrates (CH_4) and contact metamorphism of organic carbon-rich sediments (Retallack and Jahren,

40   2008; Svensen et al., 2009) are likely to have contributed additional volatiles into the atmosphere, thus deeply altering the

41   climate and the chemical composition of the ocean. This presumably close chronological association has led many authors to

42   support a cause-effect relationship between flood basalt volcanism and mass extinctions. Constraining the timing and

43   duration of the PTBME in a precisely and accurately quantified model that combines relative (i.e., biostratigraphy,

44   environmental changes) and sequences of absolute (zircon geochronology) ages is key to reveal the cascading causes and

45   effects connecting rapid environmental perturbations to biological responses.

46   The South China block provides a few exceptional marine successions with a continuous stratigraphic record across the PTB

47   (e.g., Yin et al., 2014). Among these is the Global Stratotype Section and Point (GSSP) in Meishan D (Yin et al., 2001),

48   where the PTB is defined by the first occurrence (FO) of the Triassic conodont *Hindeodus parvus*. Additionally, these South

49   Chinese sections reflect intense regional volcanic activity during Late Permian and Early Triassic times as manifested by

50   many intercalated zircon-bearing ash beds (Burgess et al., 2014; Galfetti et al., 2007; Lehrmann et al., 2015; Shen et al.,

51   2011). High-precision U-Pb zircon geochronology can be applied to these ash beds by assuming that the age of zircon

52   crystallization closely approximates the age of the volcanic eruption and ash deposition. Earliest U-Pb geochronological

53   studies (e.g., Bowring et al., 1998; Mundil et al., 2004; Ovtcharova et al., 2006; Shen et al., 2011) are not sufficiently precise

54   for the calibration of magmatic and biological events. Recent improvements of the U-Pb dating technique by the

55   development of the chemical abrasion-isotope dilution-thermal ionization mass spectrometry (CA-ID-TIMS; Mattinson,

56   2005), by the revision of the natural U isotopic composition (Hiess et al., 2012), by the development of data reduction

57   software (Bowring et al., 2011; McLean et al., 2011) and by the calibration of the EARTHTIME ^{202}Pb-^{205}Pb-^{233}U-^{235}U tracer

58   solution (Condon et al., 2015) now provide more accurate weighted mean zircon population dates at the <80 ka level

59   (external uncertainty) for a PTB age, which allow for more precise calibration between biotic and geologic events during

60   mass extinctions and recoveries. Two of the cases benefiting from this improved technique is the highly condensed GSSP

61   defining the PTB at Meishan (Burgess et al., 2014) and the Early-Middle Triassic boundary in Monggan (Ovtcharova et al.,

62   2015).

63   The aim of this work is 1) to date the PTB in two sedimentary sections that are continuous and significantly more expanded

64   than Meishan, using the highly precise and accurate dating technique of CA-ID-TIMS, and 2) to test the age consistency

65 between the PTB as defined paleontologically in Meishan and as recognized by conformable formational boundaries in the

66 deeper water sections, Dongpan and Penglaitan. Our high-precision dates provide a future test for the synchronicity of

67 conodont biozones, chemostratigraphic correlations, and other proxies involved in the study of the PTBME. Moreover,

68 applying Bayesian age modeling (Haslett and Parnell, 2008) based on these high-precision data sets allows us to detect

69 sedimentary gaps and variations in sedimentation rate, and to directly compare other proxy data across different PTB

70 sections, inclusive of the Meishan GSSP.

71 Our data demonstrate that the PTB, as recognized in our sections by conformable boundaries between late Permian and basal

72 Triassic formations, is synchronous within analytical uncertainty of ca. 30 ka. We also show that Bayesian age models

73 produce reproducible results from different sections, even though U-Pb datasets originate from different laboratories. We

74 construct a coherent age model for the PTB in Dongpan and Penglaitan, which is also in agreement with the PTB age model

75 from Meishan (Burgess et al., 2014). These results further demonstrate that ^{206}Pb/^{238}U dates produced in two different

76 laboratories using the EARTHTIME tracer solution provide reproducible age information at the 0.05 % level of uncertainty.

2 Geological setting

2.1 Regional context

79 The newly investigated volcanic ash beds were sampled from two PTB sections: Dongpan in southwestern Guangxi Province

80 and Penglaitan in central Guangxi Province in South China (Fig. 1A, exact sample locations are given in Appendix A). Both

81 sections are within the Nanpanjiang Basin (Lehrmann et al., 2015), a Late Permian-Early Triassic pull-apart basin in a back

82 arc context located on the present day southern edge of the South China block. This deep-marine embayment occupied an

83 equatorial position in the Eastern Paleo-Tethys Ocean (e.g., Golonka and Ford, 2000; Lehrmann et al., 2003; Fig. 1B). The

84 basin was dominated by a mixed carbonate-siliciclastic regime during Permian and Early Triassic times and underwent a

85 major change to a flysch dominated regime in later Triassic times (e.g., Galfetti et al., 2008; Lehrmann et al, 2007). Dm-to-m

86 thick beds of mixed volcanic and clastic material as well as mm-to-cm thick volcanic ash beds are locally abundant and

87 especially well preserved in down-thrown blocks recording deep water records in low energy environments and to a lesser

88 degree, on up-thrown blocks recording shallow water to outer platform settings. Volcanic ash beds are, however, usually not

89 preserved in traction-dominated slope deposits. Genetically related volcanic rocks crop out in the south western part of the

90 basin towards Vietnam, suggesting the proximity of a volcanic arc related to the convergence between Indochina and South

91 China (Faure et al., 2016). The volcanism produced by this convergence is the most likely source of the analyzed volcanic

92 ashes (Gao et al., 2013).

93 In Dongpan and Penglaitan, the PTB is manifested by a sharp and conformable transition from the late Permian Dalong Fm.

94 (= Talung Fm.) to the basal Triassic Ziyun Fm. Late Permian rocks in these two sections are classically assigned to the

95 Dalong Fm. of Changhsingian age. However, we note that there are substantial facies differences between these two late

96 Permian records. The Dalong Fm. in Dongpan is composed of thin-bedded siliceous mudstones, numerous ash layers and

97   minor limestone beds (Fig. 2). This facies association is in agreement with the vast majority of reported occurrences of this

98   formation within the South China block. The Dalong Fm. is interpreted as a basinal depositional environment with restricted

99   circulation and an estimated water depth of 200 m to 500 m (He et al., 2007; Yin et al., 2007). In Guangxi and Guizhou, the

100 thickness of the typical Dalong Fm. is highly variable and ranges from a couple of meters to ca. 60 m. Rocks assigned to the

101 Dalong Fm. in Penglaitan markedly diverge from those of the typical Dalong Fm. In Penglaitan, rocks assigned to Dalong

102 Fm. reach an unusual thickness of ca. 650 m and are lithologically much more heterogeneous, with a marked regressive

103 episode in its middle part (Shen et al., 2007). Moreover, in Penglaitan the Dalong Fm. contains numerous volcanogenic

104 sandstones distributed within the entire succession, a distinctive feature when compared to other sections. Only the lower

105 part of the "Dalong Fm." in Penglaitan can be unambiguously assigned to this formation. The middle and upper part of this

106 section are notably shallower, showing cross bedding and ripple marks in the uppermost 30 m of the Permian, which are

107 underlain by upper shoreface to foreshore facies deposits containing coal seams and abundant plant fossils (Shen et al.,

108 2007). This disparate depositional setting is here interpreted as that of a fault-bounded block successively thrown down and

109 up. Hence, Penglaitan stands in marked contrast with the homogenous deeper water facies of the typical Dalong Fm. in other

110 sections. In Penglaitan, the topmost few meters of the Permian Dalong Fm. comprise thin bedded dark grey limestone

111 intercalated with thick volcanogenic sandstones and thin volcanic ash beds (Fig. 3).

112 The conformably overlying Early Triassic rocks have been previously assigned to the Luolou Fm. in both Penglaitan and

113 Dongpan (Feng et al., 2007; He et al., 2007; Shen et al., 2012; Zhang et al., 2006). At its type locality and elsewhere in

114 northwestern Guangxi and southern Guizhou, the base of the Luolou Fm. is invariably represented by shallow water

115 microbial limestone. In contrast, the onset of the Triassic at Dongpan and Penglaitan is represented by ca. 30 m of laminated

116 black shales overlain by several hundred meters of thin bedded, mechanically laminated, medium to light grey limestone. In

117 Dongpan, edgewise conglomerates and breccias are occasionally intercalated within the platy, thin bedded limestone unit.

118 This succession of facies illustrates a change from basinal to slope depositional environments and is identical to that of the

119 Ziyun Fm. at its type locality 3 km East of Ziyun County city, Guizhou Province (Guizhou Bureau of Geology and Mineral

120 Resources, 1987). Therefore, Early Triassic rocks in Dongpan and Penglaitan are here reassigned to the Ziyun Fm., whose

121 base is of Griesbachian age. In most sections in Guangxi and Guizhou, where latest Permian rocks are represented by the

122 Dalong Fm., these are consistently and conformably overlain by basal black shales of the Early Triassic Ziyun Fm. or Daye

123 Fm. (e.g., Feng et al., 2015). In these downthrown blocks, the effects of the Permian-Triassic global regression were

124 comparatively negligible in comparison to those observed in adjacent, up-thrown blocks that recorded pronounced

125 unconformities or condensation..

2.2 The Dongpan section

127 Numerous litho-, bio- and chemo-stratigraphic studies (e.g., Feng et al., 2007; He et al., 2007; Luo et al., 2008; Zhang et al.,

128 2006) have been published on the Dongpan section during the last two decades. However, the volcanic ash beds of this

129 continuous PTB section have never been dated. The classic lithostratigraphic subdivisions of the Dongpan section (bed 2 to

130   13; indicated on Fig. 2) (Meng et al., 2002) can easily be recognized in the field. Based on the conodont alteration index

131   (CAI), Luo et al. (2011) established that the section shows only a low to moderate thermal overprint equivalent to a maximal

132   burial temperature of 120°C. Our own estimation of the CAI of conodont elements obtained from the same beds points

133   toward values around 3, thus confirming the estimation of Luo et al. (2011).

134   Beds 2 to 5 consist of thin (dm to cm) siliceous mudstones, mudstones, minor lenticular limestone horizons and numerous

135   intercalated volcanic ash beds. These beds yield radiolarians, foraminifera (Shang et al., 2003), bivalves (Yin, 1985),

136   ammonoids (Zhao et al., 1978), brachiopods (He et al., 2005), ostracods (Yuan et al., 2007), and conodonts (Luo et al., 2008)

137   of Changhsingian age. Chinese authors have provided very detailed studies of radiolarian occurrences from the top of the

138   Dongpan section, documenting about 160 species belonging to 50 genera (Feng et al., 2007; Wu et al., 2010; Zhang et al.,

139   2006). Most of these radiolarians belong to the *Neoalbaillella optima* assemblage zone of Late Changhsingian age (Feng and

140   Algeo, 2014), although it is unclear if some of the Permian taxa reported from the top of the section by previous authors (i.e.

141   above bed 6, Feng et al., 2007) still belong to this assemblage or to a provisional ultimate Permian biozone (Xia et al., 2004).

142   We collected five samples with visible radiolarians (DGP-1 to DGP-5, see Fig. 2) for this study. Our goal was not to

143   duplicate the detailed faunal studies performed at Dongpan by previous authors, but essentially was to correlate these

144   previous results with our U-Pb ages using own radiolarian data. A selection of well-preserved taxa is illustrated in Appendix

145   C. We also report the occurrence of morphotypes belonging to the genus *Hegleria* which was previously reported from the

146   section but not illustrated. Our data confirm that radiolarians of the Dongpan section belong to the *Neoalbaillella optima*

147   assemblage zone.

148   The conodont fauna obtained from beds 3 and 5 was assigned to the *Neogondolella yini* interval zone by Luo et al. (2008).

149   *Neogondolella yini* is also a characteristic species of the UAZ1 zone, which is the oldest zone of a new high accuracy

150   zonation around the PTB constructed by means of unitary associations (Brosse et al., 2016). Bed 6 is composed of a yellow

151   fine-grained volcanic ash bed and thin-bedded siliceous mudstone. Beds 7 to 12 contain more frequent mudstone and yield a

152   diverse Permian fauna (Feng et al., 2007; He et al., 2007; Yin et al., 2007). Additionally, He et al. (2007) showed that end-

153   Permian brachiopods underwent a size reduction in the upper-most beds of the Dalong Fm., which they linked with a

154   regressive trend.

155   The sharp and conformable base (bed 13) of the Early Triassic Ziyun Fm. consists of brown-weathering black shales

156   containing a few very thin (mm-to-cm) volcanic ash beds and volcanogenic sandstones. Previous studies did not recognize

157   how recent weathering superficially altered these black shales. Bed 13 contains abundant bivalves and ammonoids of

158   Griesbachian age (Feng et al., 2007; He et al., 2007), which are also known from other sections where the equivalent black

159   shales are not weathered. Therefore, the formational boundary placed between beds 12 and 13 is reasonably well constrained

160   in terms of paleontological ages. Even in the absence of any close conodont age control, this boundary has been unanimously

161   acknowledged as the PTB in all previous contributions, thus emphasizing the significance of this formational change.

2.3 The Penglaitan section

The Penglaitan section is well known for its Guadalupian-Lopingian boundary (Capitanian-Wuchiapingian GSSP; Jin et al., 2006; Shen et al., 2007). However, the part of the section that straddles the PTB has not been the focus of any detailed published work. Shen et al. (2007) report Changhsingian *Peltichia zigzag-Paryphella* brachiopod assemblage from a volcanogenic sandstone bed at ~28 m below the PTB. In addition, *Palaeofusulina sinensis* is abundant in the uppermost limestone units of the Dalong Fm. and conodonts in the topmost part were assigned to the *Clarkina yini* Zone. A poorly preserved Permian nautiloid was recovered from the volcanogenic sandstone 1.3 m below the PTB (Fig. 3). About 0.3 m above the PTB, concretionary, thin-bedded micritic layers intercalated within the basal black shales of the Ziyun Fm. yielded one P1 element of *Hindeodus parvus* (Fig. 3). Pending the age confirmation of new paleontological data, and in full agreement with Shen et al. (2007), we place the PTB at this sharp but conformable formational boundary.

3 Methods

3.1 CA-ID-TIMS analysis

Sample preparation, chemical processing and U-Pb CA-ID-TIMS zircon analyses were carried out at the University of Geneva. Single zircon grain dates were produced relative to the EARTHTIME ^{202}Pb-^{205}Pb-^{233}U-^{235}U tracer solution (Condon et al., 2015). All uncertainties associated with weighted mean ^{206}Pb/^{238}U ages are reported at the 95 % confidence level and given as ±x/y/z, with x as analytical uncertainty, y including tracer calibration uncertainty, and z including ^{238}U decay constant uncertainty. The tracer calibration uncertainty (y) of 0.03 % (2σ) has to be added if the calculated dates are to be compared with other U-Pb laboratories not using the EARTHTIME tracer solution. The ^{238}U decay constant uncertainty (z) of 0.11 % (2σ) should be used if compared with other chronometers such as Ar-Ar. All ^{206}Pb/^{238}U single grain ages have been corrected for initial ^{230}Th-^{238}U disequilibrium assuming Th/U$_{magma}$ of 3.00 ± 0.50 (1σ). Th-corrected ^{206}Pb/^{238}U dates are on average 80 ka older than the equivalent uncorrected dates when applying this correction and are presented as mean ages of selected zircon populations and their associated ±2-sigma uncertainties in Figs. 2 and 3, and as single grain ^{206}Pb/^{238}U age ranked distribution plots in Fig. 4. The full data table and analytical details are given in Appendix B.

3.2 Bayesian chronology

In this study we use Bayesian interpolation statistics to establish a probabilistic age model based on our high-precision U-Pb zircon dates of each individual ash bed and its stratigraphic position, as it is incorporated in the free Bchron R software package (Haslett and Parnell, 2008; Parnell et al., 2008) to constrain the chronological sequence and sedimentation history of the investigated sections. By assuming normal distribution of our U-Pb dates within one sample, and based on the principle of stratigraphic superposition, which requires that any stratigraphic point must be younger than any point situated below in the stratigraphic sequence, it models the age and its associated 95 % confidence interval for any depth point within the studied sedimentary sequence. The model is based on the assumption of constant sedimentation rates, which is allowed to

193   change several times between each dated stratigraphic point. The number of such changes is modeled by a Poisson

194   distribution, and the size of the sedimentation rates by a gamma distribution. The strength of this approach is its flexibility

195   that allows changes in sedimentation rate from zero (hiatus in sedimentation) to very large values (sedimentation event at

196   high rate). In contrast to standard linear regression models, this approach leads to more realistic uncertainty estimates, with

197   increasing uncertainty at growing stratigraphic distance from the dated layers. The model also detects and excludes outliers,

198   which conflict with other evidence from the same sequence in order to produce a coherent and self-consistent chronology; no

199   predefined outlier determination is required from the user. One of the drawbacks of this Bayesian approach is that a change

200   in the sedimentation rate is assumed to occur at each dated stratigraphic position, though it is unlikely that the change in

201   sedimentation occurs exactly at the depth of a dated bed. Another drawback is that the sedimentation parameters are shared

202   across the whole sequence. In consequence, Bchron does not allow much opportunity for users to individually influence the

203   chronology behaviour.

204   In this study we use the Bayesian Bchron model as it is part of the Bchron package (http://cran.r-

205   project.org/web/packages/Bchron/index.html). This model outperforms other Bayesian age depth-models, as shown by a

206   extensive comparison conducted on radiocarbon dates from Holocene lake sediments (Parnell et al., 2011). It provides a non-

207   parametric chronological model according to the Compound Poisson-Gamma model defined by Haslett and Parnell (2008),

208   requiring the weighted mean $^{206}Pb/^{238}U$ age, the stratigraphic position and the thickness of the investigated ash beds as input

209   parameters. The technical details were given in Haslett and Parnell (2008). The Bchron model uses a Markov Chain Monte

210   Carlo (Brooks et al., 2011) rejection algorithm which proposes model parameters and accepts or rejects them in order to

211   produce probability distributions of dates for a given depth that match likelihood and do not violate the principle of

212   stratigraphic superposition. In order to create an adequate number of accepted samples, the model was run for 10,000

213   iterations.

214   **4 Samples**

215   In total, 12 volcanic ash beds and volcanogenic sandstones were sampled from the Dalong Fm. of Late Permian age and

216   from the overlying Ziyun Fm. of Early Triassic age at Dongpan and Penglaitan (see Appendix A). Most of the dated samples

217   exhibit $^{206}Pb/^{238}U$ age dispersions that exceed the acceptable scatter from analytical uncertainty and are interpreted as

218   reflecting magmatic residence or a combination of the latter with sedimentary recycling. Only in two cases (DGP-16, PEN-

219   22) we find single grain analyses younger than our suggested mean age and interpret them as unresolved Pb loss since they

220   strongly violate the stratigraphic order established by the chronology of the volcanic ash beds.

221   At Dongpan, six fine- to medium-grained volcanic ash beds (DGP-10, DGP-11, DGP-12, DGP-13, DGP-16 and DGP-17) in

222   the upper-most 10 m of the Dalong Fm., one fine-grained ash bed (DGP-21) just 10 cm above the base of the Ziyun Fm., and

223   one thin-bedded volcanogenic sandstone (DGP-18) 40 cm stratigraphically higher were collected for geochronology. At

224   Penglaitan, the basal part of a 25 cm thick volcanogenic sandstone (PEN-6), one thin-layered volcanic ash bed (PEN-70) and

225   the base of a 30 cm thick volcanogenic sandstone (PEN-28), all together representing the upper-most 1.1 m of the Dalong

226 Fm., were dated. A single fine-grained and extremely thin (2-3 mm) volcanic ash bed (PEN-22) was sampled 50 cm above

227 the base of the Ziyun Fm. and thus closely brackets the formational boundary. U-Pb CA-ID-TIMS geochronology following

228 procedures described above and in the appendix was applied to a number of single crystals of zircon extracted from these

229 volcanic ash beds. Trace element and Hf isotopic compositions of these dated zircons will be presented elsewhere.

230 Stratigraphic positions of volcanic ash beds at Dongpan and Penglaitan and weighted mean $^{206}Pb/^{238}U$ dates of individual

231 zircon grains for the samples below are given in Fig. 2 and Fig. 3.

5 Results

233 The U-Pb isotopic results are presented in Fig. 4 as $^{206}Pb/^{238}U$ age ranked plots for each individual sample, and in Table B1

234 (Appendix).

5.1 U-Pb age determinations from the Dongpan section

5.1.1 Sample DGP-10

237 This volcanic ash bed was sampled 9.7 m below the formational boundary. All ten dated zircons are concordant within

238 analytical error, where the seven youngest grains define a cluster with a weighted mean $^{206}Pb/^{238}U$ age of 252.170 ±

239 0.055/0.085/0.28 Ma (mean square of weighted deviates [MSWD] = 1.18) for the deposition of DGP-10.

5.1.2 Sample DGP-11

241 This volcanic ash bed was sampled 7.9 m below the formational boundary. Eleven zircon crystals were analyzed, resulting in

242 scattered $^{206}Pb/^{238}U$ dates of 251.662 ± 0.263 Ma to 252.915 ± 0.352 Ma. The six youngest zircons yield a weighted mean

243 $^{206}Pb/^{238}U$ age of 251.924 ± 0.095/0.12/0.29 Ma (MSWD = 1.80) that is too young with respect to the stratigraphic sequence

244 defined by over- and underlying ash beds. Therefore, we have to assume that abundant unresolved lead loss affected these

245 zircons, despite application of the same chemical abrasion procedure as for all other samples. It is worth noting that all

246 zircons from DGP-11 were almost completely dissolved after chemical abrasion and show elevated $^{206}Pb/^{238}U$ age

247 uncertainties of ~0.30 Ma compared to other volcanic ash beds from Dongpan.

5.1.3 Sample DGP-12

249 This volcanic ash bed was sampled 7.3 m below the formational boundary. The weighted mean age of 252.121 ±

250 0.035/0.074/0.28 Ma (MSWD = 1.04) is derived from eight concordant grains representing the youngest zircon population of

251 this ash bed.

5.1.4 Sample DGP-13

This volcanic ash bed was sampled 6.4 m below the formational boundary. Analyses of seven individual zircons yield a statistically significant cluster with a weighted mean $^{206}Pb/^{238}U$ age of 251.101 ± 0.037/0.075/0.28 Ma (MSWD = 0.67) representing the youngest zircon population of this ash bed.

5.1.5 Sample DGP-16

This volcanic ash bed was sampled 3.2 m below the formational boundary. Nine zircons yield a weighted mean $^{206}Pb/^{238}U$ age of 251.978 ± 0.039/0.076/0.28 Ma (MSWD = 0.66). The youngest grain shows unresolved lead loss and was discarded because it strongly violates the stratigraphic superposition. Incorporating this zircon into the mean age calculation would also lead to a statistically flawed MSWD of 4.80.

5.1.6 Sample DGP-17

This volcanic ash bed was sampled 2.7 m below the formational boundary. A total of 11 zircons define a weighted mean $^{206}Pb/^{238}U$ age of 251.956 ± 0.033/0.073/0.28 Ma (MSWD = 0.96). One single zircon displays inheritance with an $^{206}Pb/^{238}U$ age of 252.896 ± 0.108 Ma and was consequently excluded from the weighted mean age calculation.

5.1.7 Sample DGP-21

This volcanic ash bed was sampled 0.1 m above the formational boundary. 14 zircons were dated, among which the eight youngest yield a cluster with a weighted mean $^{206}Pb/^{238}U$ age of 251.953 ± 0.038/0.075/0.28 Ma (MSWD = 0.26). The six oldest grains display an inherited component as suggested by their scattered $^{206}Pb/^{238}U$ dates ranging from 252.145 ± 0.120 Ma to 252.715 ± 0.084 Ma. The U-Pb data of DGP-21 was already published in a companion study (Baresel et al., in press) that deals with the stratigraphic correlation of ash beds straddling the PTB in deep- and shallow-marine successions of the Nanpanjiang Basin.

5.1.8 Sample DGP-18

This bed was sampled 0.5 m above the formational boundary. The re-sedimented nature of this volcaniclastic bed is reflected in the $^{206}Pb/^{238}U$ zircon ages ranging from 252.559 ± 0.261 Ma to 257.274 ± 0.689 Ma. This sample was excluded from the age-depth model, because it clearly violates the stratigraphic superposition.

5.2 U-Pb age determinations from the Penglaitan section

5.2.1 Sample PEN-6

PEN-6 comes from the base of a volcanogenic sandstone. It was sampled 1.1 m below the formational boundary. Fifteen zircon grains were dated. The three youngest grains define a weighted mean $^{206}Pb/^{238}U$ age of 251.137 ± 0.082/0.11/0.29 Ma

280   (MSWD = 0.13). Because zircon dates from this bed spread over almost 2 Ma, recycling of older volcanic material via
281   sedimentary processes appears more likely than via magmatic recycling.

5.2.2 Sample PEN-70

283   This volcanic ash bed was sampled 0.6 m below the formational boundary. Eighteen zircon grains were analyzed. As in the
284   case of PEN-6, they yield a scatter of $^{206}Pb/^{238}U$ dates spanning 1.5 Ma, ranging from 251.994 ± 0.169 Ma to 253.371 ±
285   0.165 Ma. The weighted mean age of 252.125 ± 0.069/0.095/0.29 Ma (MSWD = 0.59) for the deposition of this ash bed is
286   calculated by using the seven youngest concordant grains.

5.2.3 Sample PEN-28

288   This sample was taken 0.3 m below the formational boundary. It is derived from the base of a 30 cm thick volcanogenic
289   sandstone which represents the youngest Permian bed in Penglaitan. Analyses of seven zircon grains yield a cluster with a
290   weighted mean $^{206}Pb/^{238}U$ age of 252.062 ± 0.043/0.078/0.28 Ma (MSWD = 0.49), reflecting the last crystallization phase of
291   this zircon population. Six older grains ranging from 252.364 ± 0.156 Ma to 253.090 ± 0.375 Ma indicate either magmatic or
292   sedimentary recycling. The U-Pb data of PEN-28 was already published in Baresel et al. (in press).

5.2.4 Sample PEN-22

294   This 2 mm thick volcanic ash bed was sampled 0.5 m above the formational boundary. Eight zircons yield a weighted mean
295   $^{206}Pb/^{238}U$ age of 251.907 ± 0.033/0.073/0.28 Ma (MSWD = 0.10). One zircon grain shows a significantly younger age
296   suggesting lead loss. Two slightly older grains reflect noticeable pre-eruptive crystallization. Incorporation of these grains
297   into the weighted mean calculation would lead to an excessive MSWD of 3.6 and 1.9, respectively.
298   However, we noticed that some volcanic ash beds and volcanogenic sandstones in these sections show a large age dispersion
299   of up to 2 Ma, incompatible with recycling of zircon that previously crystallized within the same magmatic system and
300   became recycled into later melt batches, leading to few 100 ka dispersion of dates (e.g., Broderick et al., 2015; Samperton et
301   al., 2015), but pointing to sedimentary reworking. The U-Pb data of PEN-22 was already published in Baresel et al. (in
302   press).

5.3 Age-depth models

304   Figure 5 shows a comparison of three different age-depth models based on linear interpolation, cubic spline interpolation and
305   Bayesian statistics, each applied to exactly the same U-Pb dataset of Dongpan (Fig. 5a) and Penglaitan (Fig. 5b). It is visible
306   that, the Bayesian Bchron model produces a slightly increased uncertainty of the model age with increasing distance from
307   the stratigraphic position of a U-Pb dated sample (as discussed in the Methods' section). Due to the well constrained U-Pb
308   dates of Dongpan and Penglaitan, all three age-depth models predict (within uncertainty) similar ages for the PTB in
309   Dongpan (Fig. 5a) and Penglaitan (Fig. 5b). Given that the Bayesian Bchron model evaluates the age probability distribution

310 of each U-Pb date with respect to the other dates of the sequence, it provides a more robust and better constrained
311 chronology, which even results in smaller uncertainties of the predicted model dates compared to the standard linear
312 regression models (as indicated by the smaller uncertainty of the Bchron model age for the PTB in Dongpan and Penglaitan).
313 In contrast to the other two models, the Bayesian Bchron model can identify U-Pb dates that violate the principle of
314 stratigraphic superposition, as shown for the Dongpan ash beds DGP-11 (outlier probability of 67 %) and DGP-18 (outlier
315 probability of 100 %). Including them into the age-depth chronology of Dongpan results in unrealistic negative
316 sedimentation rates, as reflected by the linear and cubic interpolation models for the interval between DGP-11 and DGP-12,
317 and for the interval between DGP-21 and DGP-18 (Fig. 5a).
318 The aim for applying Bayesian age modelling to the dated volcanogenic beds from these two sections was to obtain an age
319 model for the PTB. The age-depth models yield ages of 251.938 ± 0.029 Ma (Dongpan; Fig. 2; Fig. 5a) and of 251.982 ±
320 0.031 Ma (Penglaitan; Fig. 3; Fig. 5b) for the lithological boundary between the Dalong and Ziyun Fm. in both sections.
321 These two ages overlap within uncertainties and thus demonstrate the synchronicity of the PTB in the two sections. Making
322 the reasonable assumption of absence of significant gaps in these two sections, the new U-Pb dates can be used to infer
323 sedimentation rates. The age-depth model of Dongpan suggests increased sedimentation rates in the upper-most part of the
324 Dalong Fm. from bed 6 (DGP-17) upwards. Below bed 6, calculated sedimentation rates appear to be relatively constant
325 with 3.6 ± 1.2 cm ka^{-1}, but above bed 6 they jump to 6.0 ± 2.4 cm ka^{-1}. In Penglaitan, the sedimentation rate of the upper-
326 most Dalong Fm. and basal-most Ziyun Fm. is significantly lower than in Dongpan with 0.7 ± 0.3 cm ka^{-1}. Previously
327 published U-Pb zircon geochronology from Penglaitan (Shen et al., 2011), including a weighted mean date of 252.16 ± 0.09
328 Ma from a volcanogenic sandstone at 26.7 m below the PTB, was not considered in our age model, since substantial
329 improvements in the analytical protocol hamper comparing these dates with our U-Pb results.

6 Comparison of the Dongpan and Penglaitan sections with Meishan GSSP Results

6.1 The change of the PTB age through analytical improvement of U-Pb dating

332 The first geochronological studies in the GSSP Meishan D have been carried out on bed 25, immediately underlying the
333 PTB, by U-Pb sensitive high-resolution ion microprobe (SHRIMP) analysis of zircons yielding a ^{206}Pb/^{238}U age of 251.2 ±
334 3.4 Ma (Claoué-Long et al., 1991) and by ^{40}Ar/^{39}Ar dating of sanidine at 249.91 ± 0.15 Ma (Renne et al., 1995). However,
335 these dates are either not sufficiently precise to allow calibrating magmatic and biological timescales at resolution adequate
336 for both groups of processes, or are biased by a systematic age offset between the U-Pb and Ar-Ar systems of ~1.0 %
337 (Schoene et al., 2006). In order to properly compare the two systems, all older ^{40}Ar/^{39}Ar data have to be corrected for the
338 revised age of the standard Fish Canyon sanidine of 28.201 ± 0.046 Ma (Kuiper et al., 2008) and the decay constant
339 uncertainty has to be added to U-Pb and Ar-Ar ages which would drastically expand the ^{40}Ar/^{39}Ar age error and recalculate
340 the ^{40}Ar/^{39}Ar age of Renne et al. (1995) to 252.1 ± 1.6 Ma. In a first detailed ID-TIMS study, U-Pb ages of mechanically
341 abraded zircons were published by Bowring et al. (1998) for six volcanic ash beds at Meishan, placing the PTB at 251.4 ±

342   0.3 Ma. Though much more precise than former studies, these ages are mainly based on multi-grain zircon analyses. That

343   this approach might disguise complexity of zircon population ages, as pervasive lead loss and inheritance, was shown by

344   Mundil et al. (2001) by confining data selection to single-crystal analyses of the same horizons. In a second attempt, driven

345   by further improvements of the U-Pb ID-TIMS technique (e.g., chemical abrasion of zircon grains by hydrofluoric acid

346   exposure to remove zircon domains with lead loss; reduced procedural common Pb blanks), the PTB extinction horizon in

347   Meishan and Shangsi (China) was dated at 252.6 ± 0.2 Ma by Mundil et al. (2004). Unlike previous studies, Shen et al.

348   (2011) dated larger number of zircon grains per ash bed in order to overcome inheritance, magmatic residence, and lead loss

349   phenomena of zircon population ages. They determined the duration of the PTB extinction interval (bed 25 to bed 28 in

350   Meishan) at 200 ± 100 k.y. starting at 252.28 ± 0.08 Ma in bed 25 together with a sharp negative $\delta^{13}C$ excursion. By using

351   the same mineral separates from identical ash beds as in Shen et al. (2011), the extinction period at Meishan was determined

352   by Burgess et al. (2014) between 251.941 ± 0.037 Ma (bed 25) and 251.880 ± 0.031 Ma (bed 28). The differences in age and

353   precision compared to Shen et al. (2011) reflect significant progress of the EARTHTIME community in data acquisition and

354   reduction such as refined tracer calibration, new error propagation algorithms, and the development of the EARTHTIME

355   ^{202}Pb-^{205}Pb-^{233}U-^{235}U tracer solution.

356   Figure 6 illustrates the three Bayesian age-depth models based on our U-Pb dates from Dongpan and Penglaitan compared to

357   the latest generation of U-Pb ages from Meishan GSSP (Burgess et al. 2014). Such a comparison is possible because all the

358   dates from these three sections were obtained with the same analytical procedures, including identical data reduction

359   procedures, error propagation and Th correction, thus leading to closely comparable precision and accuracy of the ages. This

360   tight temporal framework allows us to perform a quantitative comparison of the Dongpan, Penglaitan and Meishan sections

361   in terms of lithostratigraphy, biostratigraphy and chemostratigraphy via the Bayesian statistics.

6.2 Comparison of lithostratigraphy

363   All three interpolated ages of the formational boundary in Dongpan (251.938 ± 0.029 Ma), Penglaitan (251.982 ± 0.031 Ma)

364   and Meishan (251.956 ± 0.033 Ma) are in agreement within errors (Fig. 6). They support the synchronicity of the

365   conformable boundary between the Dalong Fm. and the Ziyun Fm. in Dongpan and Penglaitan, and also demonstrate their

366   temporal coincidence with the conformable boundary in Meishan between the Changhsing Fm. and Yinkeng Fm. The age

367   model also confirms the extreme condensation around the PTB in Meishan, with a maximal sedimentation rate of 0.4 cm ka^{-1}

368   as reported by Burgess et al. (2014) for the 26 cm thick interval bracketed by beds 25 and 28. In this respect, Dongpan and

369   Penglaitan offer a greater potential for higher resolution studies of environmental proxies around the PTB with maximal

370   sedimentation rates for the same interval of 8.4 cm ka^{-1} and 1.0 cm ka^{-1}, respectively. The increased sedimentation rate above

371   bed 6 in Dongpan is in agreement with the previously inferred sedimentary fluxes deduced from elemental chemical analyses

372   (Shen et al., 2012). From bed 7 upward, He et al. (2007) showed a clear increase of Al_2O_3 and TiO_2 indicating increased

373   fluxes of terrestrial input into this trough. The accompanying size reduction of brachiopods (He et al., 2007) led them to infer

374   a regressive trend in the upper part of the Dongpan section. The ecological consequences of any regressive trend or increased

375 clastic input might conceivably impact the diversity of marine species but distinguishing between increased fluxes and

376 regression remains difficult because both causes may have converging consequences.

377 **6.3 Comparison of biostratigraphy**

378 The PTB is defined by the FO of *H. parvus* in the GSSP Meishan D in bed 27c. This definition is complicated by the

379 suggested existence of a hardground within bed 27, which is at the position of the previously defined PTB (Chen et al.,

380 2009). Others have suggested that the FO of *H. parvus* at Meishan is not the timing of the true evolutionary origination of

381 this species (Jiang et al., 2011; Yuan et al., 2015). In Meishan, the FO of *H. parvus* in bed 27c is interpolated at 251.892 ±

382 0.045 Ma (Fig. 6) and is located 21 cm above the formational boundary which occurs between beds 24 and 25. Temporally

383 coincident, the FO of *H. parvus* in Penglaitan is interpolated at 251.929 ± 0.032 Ma (Fig. 6) and is located 33 cm above the

384 formational boundary. With respect to formational boundaries, the higher stratigraphic position of the FO of *H. parvus* in

385 Penglaitan than in Meishan is to be expected because of the higher sedimentation rate. However, in Meishan *H. parvus* first

386 occurs 64 ± 56 k.y. after the formational boundary and in Penglaitan after 53 ± 46 k.y., indicating perfect synchronicity

387 within our temporal resolution. In Dongpan, the lack of conodont bearing beds around the PTB hampers testing the

388 synchronicity of the FO of *H. parvus* between Dongpan and the two other sections.

389 Brosse et al. (2016) established a new and robust conodont zonation based on unitary associations around the PTB in South

390 China that includes the Meishan GSSP. This zonation contains six Unitary Association Zones (UAZ), with the PTB falling

391 into the separation interval between UAZ2 (bed 25) and UAZ3 (bed 27a-d). This new zonation also places the UAZ-based

392 PTB in Meishan closer to the conformable boundary between the Changhsing and the Yinkeng formations than the FO of H.

393 parvus (bed 27c) does. Available conodont data from Meishan allow the assignment of bed 24a-e to UAZ1 (UAZ1 might

394 reach further down as indicated by a dashed line in Fig. 6), bed 25 to UAZ2, bed 27a-d to UAZ3 and bed 28 to UAZ4

395 (Brosse et al., 2016). The stratigraphic thickness comprised between the base of UAZ1 and the top of UAZ4, amounts to

396 1.22 m. By using the three section age-depth models, we attempted to project the respective thickness corresponding to the

397 UAZ1-UAZ4 interval in Meishan onto the two other sections. This projection resulted into a pronounced, artificial

398 lengthening of UAZs in Dongpan and Penglaitan. UAZ1 is the penultimate Permian conodont UAZ in Meishan (Brosse et

399 al., 2016). When projected onto the age-depth models of Dongpan and Penglaitan, this UAZ1 is artificially expanded and

400 even crosses the PTB in Penglaitan (Fig. 6). In Penglaitan, the last Permian UAZ2 projects correctly above UAZ1 without

401 overlap but is completely within the Triassic. The cause of these contradictions stems from the irreconcilable conjunction of

402 i) extreme condensation in Meishan, ii) high evolutionary rates of conodonts, and iii) the ca. 30 ka precision of the last

403 generation of U-Pb dates.

404 In Dongpan, the onset of a protracted radiolarian diversity decline in bed 5 reported by Feng and Algeo (2014) is here

405 interpolated at 251.990 ± 0.027 Ma, occurring 52 ± 40 k.y. before the formational boundary (Fig. 2). Excess SiO_2 values of

406 this bed (Shen et al., 2012) suggest a genuine diversity pattern at the local scale, which seems to be unrelated to any

407 substantial change or trend in the local redox conditions (as shown by Co/Al, Cr/Al, Cu/Al and V/Al measurements of He et
408 al., 2007).

6.4 Comparison of chemostratigraphy

410 Organic carbon isotope chemostratigraphy of Dongpan (Fig. 7) extending from the Permian bed 5 to the Triassic bed 13 was
411 provided by Zhang et al. (2006) and for Meishan (Fig. 7) extending from the Permian bed 24 to the Triassic bed 29 by Cao et
412 al. (2002). The correlation of these $\delta^{13}C_{org}$ records by Zhang et al. (2006), based on the occurrence of ash beds in both
413 sections, is largely over-interpreted. With the exception of a short negative excursion followed by a more prominent positive
414 excursion between beds 9 and 11, the Permian part of the $\delta^{13}C_{org}$ record in Dongpan is relatively stable and oscillates
415 between -28 ‰ and -27 ‰. With the exception of a negative excursion culminating in beds 25 and 26, the Permian part of
416 the $\delta^{13}C_{org}$ record in Meishan shows a sustained positive trend from -30 ‰ to -26 ‰. The basal Triassic part of these two
417 records is also incompatible in that they display opposed trends. With the possible exception of the Xinmin section (Shen et
418 al., 2013a), the $\delta^{13}C_{org}$ record of Dongpan does not correlate with that of any other South Chinese section, but even Xinmin
419 shows a ~3 ‰ offset of the base trend in comparison to Dongpan. However, we note that in Meishan an abrupt decline in
420 $\delta^{13}C_{carb}$ occurs in bed 24e at 251.950 ± 0.042 Ma (Burgess et al., 2014) and slightly above in bed 26 in $\delta^{13}C_{org}$ at 251.939 ±
421 0.032 Ma, which is temporally coincident with the main negative $\delta^{13}C_{org}$ excursion in bed 9 in Dongpan at 251.954 ± 0.027
422 Ma. The second smaller negative $\delta^{13}C_{org}$ excursion at the PTB in Dongpan at 251.942 ± 0.028 Ma and in Meishan at
423 251.892 ± 0.045 Ma cannot be distinguished within uncertainty from the main excursion, which hampers the correlation of
424 the $\delta^{13}C_{org}$ records based on U-Pb ages. However, interpreting organic carbon records requires the simultaneous analysis of
425 palynofacies, which are not documented in Dongpan. Shen et al. (2012) also showed that the total organic carbon (TOC)
426 never exceeds 0.2 %, thus indicating a generally poor preservation of the organic matter in this section. As shown by Shen et
427 al. (2012), this preservation bias is further supported by coincident peaks in both terrestrial (spore and pollens) and marine
428 (algae and acritarchs) organic material (see Fig. 7). This uneven preservation of the organic matter further hampers the
429 understanding of the $\delta^{13}C_{org}$ signal in Dongpan. More generally, the consistency and lateral reproducibility of the Late
430 Permian carbonate and organic carbon isotope records in South China remain equivocal (e.g., Shen et al., 2013b). These
431 records are probably influenced by the local graben and horst paleotopography that hampered efficient circulation of water
432 masses with the open ocean, thus reflecting more local than global changes.

7 Conclusions

434 • The comparison of our high-precision U-Pb zircon data from Dongpan and Penglaitan sections in South China with the
435 data of Burgess et al. (2014) from Meishan D GSSP provides convincing evidence that dates elaborated through the use of
436 the EARTHTIME ^{202}Pb-^{205}Pb-^{233}U-^{235}U tracer solution are comparable at the 0.05 % level or better even if coming from
437 different laboratories. This fact underlines a substantially increased accuracy and precision of U-Pb ID-TIMS dating, now
438 capable to elucidate environmental change and biotic response on a decamillennial scale.

439 • Applying Bayesian age modelling to sections with such high-precision time information allows to compare disparate

440 information from different sections, quantitatively. Along with the work of Ovtcharova et al. (2015) at the Early-Middle

441 Triassic boundary, these are the two first proof-of-concept studies adopting age-depth modelling to compare coeval sections

442 with different fossil contents, different facies and disparate sedimentation rates at highest temporal resolution. We anticipate

443 that this approach will need to become the future standard in the assessment of the Geologic Time Scale.

444 • Bchron age-depth models demonstrate synchronicity of the conformable lithological boundaries in Dongpan, Penglaitan,

445 and Meishan. These results highlight the temporal reliability of the environmental changes as expressed by formational

446 boundaries in platform-slope and deeper water basinal sections.

447 • The reappraisal of the PTB in South China based on conodont Unitary Associations zones (Brosse et al., 2016) coincides

448 with the PTB age of Dongpan, and favours this characterization of the PTB over the classical definition by the FO of *H.*

449 *parvus*.

450 • The higher sedimentation rates of Dongpan and Penglaitan provide a much better prospect for the high-resolution study of

451 environmental proxies around the PTB than the condensed GSSP section in Meishan. Our age-depth models also reveal that

452 the combination of condensed deposition with high evolutionary rates of conodonts and the ~30 ka resolution of the last

453 generation of U-Pb ages makes it impossible to project stratigraphic data points or intervals of Meishan onto expanded PTB

454 sections without distortions. This intrinsic problem of the Meishan GSSP section should stimulate the search of alternative

455 sections with more expanded records.

456 • The seemingly erratic Late Permian carbon isotope record in South China does not allow laterally reproducible inter-

457 calibration with the newly obtained U-Pb dates. This stands in sharp contrast with the Early Triassic carbon isotope record

458 which is of global significance (e.g., Galfetti et al., 2007).

459 **Acknowledgements**

460 The authors acknowledge financial support by the Swiss NSF through projects 200020_137630 (to U.S.) and

461 200021_135446 (to H.B.). Aymon Baud (Lausanne) is thanked for its support in the field. Tom Algeo (Cincinnati) and Shen

462 Shuzhong (Nanjing) are thanked for insightful discussions and for providing Excel tables of carbon isotopic data from

463 published sections. A special thanks goes to technical and scientific members of the Geneva and Zürich research groups,

464 who helped during all stages of this study.

465 **References**

466 Algeo, T.J., and Twitchett, R.J.: Anomalous Early Triassic sediment fluxes due to elevated weathering rates and their

467 biological consequences. Geology, 38, 1023–1026, doi:10.1130/G31203.1, 2010.

468 Alroy, J., Aberhan, M., Bottjer, D.J., Foote, M., Fürsich, F.T., Harries, P.J., Hendy, A.J.W., Holland, S.M., Ivany, L.C.,
469   Kiessling, W., Kosnik, M.A., Marshall, C.R., McGowan, A.J., Miller, A.I., Olszewski, T.D., Patzkowsky, M.E.,
470   Peters, S.E., Villier, L., Wagner, P.J., Bonuso, N., Borkow, P.S., Brenneis, B., Clapham, M.E., Fall, L.M., Ferguson,
471   C.A., Hanson, V.L., Krug, A.Z., Layou, K.M., Leckey, E.H., Nürnberg, S., Powers, C.M., Sessa, J.A., Simpson, C.,
472   Tomasovych, A., and Visaggi, C.C.: Phanerozoic trends in the global diversity of marine invertebrates. Science, 321,
473   97–100, doi:10.1126/science.1156963, 2008.

474 Baresel, B., D'Abzac, F.X., Bucher, H., and Schaltegger, U.: High-precision time-space correlation through coupled apatite
475   and zircon tephrochronology: an example from the Permian-Triassic boundary in South China. Geology,
476   doi:10.1130/G38181.1, *in press*.

477 Benton, M.J.: The origins of modern biodiversity on land. Phil. Trans. Roy. Soc. Lond. B, 365, 3667–3679,
478   doi:10.1098/rstb.2010.0269, 2010.

479 Bowring, S.A., Erwin, D.H., Jing, G.Y., Martin, M.W., Davidek, K., and Wang, W.: U/Pb zircon geochronology and tempo
480   of the end-Permian mass extinction. Science, 280, 1039–1045, doi:10.1126/science.280.5366.1039, 1998.

481 Bowring, J.F., McLean, N.M., and Bowring, S.A.: Engineering cyber infrastructure for U-Pb geochronology: tripoli and U-
482   Pb_Redux. Geochem. Geophys. Geosyst., 12, 6, doi:10.1029/2010gc003479, 2011.

483 Broderick, C., Wotzlaw, J.-F., Frick, D., Gerdes, A., Günther, D., and Schaltegger, U.: Linking the thermal evolution of an
484   upper crustal intrusion to its lower-crustal roots using zircon and titanite geochronology and geochemistry (Southern
485   Adamello batholith, N. Italy). Contrib. Mineral. Petr., 170, 28, doi:10.1007/s00410-015-1184-x, 2015.

486 Brooks, S., Gelman, A., Jones, G., and Meng, X.-L. (Eds.): Handbook of Markov Chain Monte Carlo. Boca Raton, Florida,
487   CRC Press, 619 p., 2011.

488 Brosse, M., Bucher, H., and Goudemand, N.: Quantitative biochronology of the Permian-Triassic boundary in South China
489   based on conodont Unitary Associations. Earth-Sci. Rev., 155, 153–171, doi:10.1016/j.earscirev.2016.02.003, 2016.

490 Burgess, S.D., Bowring, S.A., and Shen, S.Z.: High-precision timeline for Earth's most severe extinction. P. Natl. Acad. Sci.
491   USA, 111, 3316–3321, doi:10.1073/pnas.1317692111, 2014.

492 Burgess, S.D., and Bowring, S.A.: High-precision geochronology confirms voluminous magmatism before, during, and after
493   Earth's most severe extinction. Sci. Adv., 1, 1–14, doi:10.1126/sciadv.1500470, 2015.

494 Cao, C.Q., Wang, W., and Jin, Y.: Carbon isotope variation across Permian-Triassic boundary at Meishan section in
495   Zhejiang province, China. Bulletin of Sciences (Chinese edition), 47, 302–306, doi:10.1360/02tb9252, 2002.

496 Chen, J., Beatty, T.W., Henderson, C.M., and Rowe, H.: Conodont biostratigraphy across the Permian-Triassic boundary at
497   the Dawen section, Great Bank of Guizhou, Guizhou Province, South China: implications for the Late Permian
498   extinction and correlation with Meishan. J. Asian Earth Sci., 36, 442–458, doi:10.1016/j.jseaes.2008.08.002, 2009.

499 Claoué-Long, J.C., Zhang, Z.C., Ma, G.G., and Du, S.H.: The age of the Permian-Triassic boundary. Earth Planet. Sci. Lett.,
500   105, 182–190, doi:10.1016/0012-821x(91)90129-6, 1991.

501   Condon, D.J., Schoene, B., McLean, N.M., Bowring, S.A., and Parrish, R.R.: Metrology and traceability of U-Pb isotope
502   dilution geochronology (EARTHTIME Tracer Calibration Part I). Geochim. Cosmochim. Ac., 164, 464–480,
503   doi:10.1016/j.gca.2015.05.026, 2015.

504   Erwin, D.H.: The End-Permian Mass Extinction. Annu. Rev. Ecol. Syst., 21, 69–91,
505   doi:10.1146/annurev.es.21.110190.000441, 1990.

506   Erwin, D.H., Bowring, S.A., and Jin, Y.-G.: End-Permian mass-extinctions: a review. In: Koeberl, C., MacLeod, K.G.
507   (Eds.), Catastrophic events and mass extinctions: impacts and beyond. Geol. S. Am. S., 356, 353–383, doi:10.1130/0-
508   8137-2356-6.363, 2002.

509   Faure, M., Lin, W., Chu, Y., and Lepvrier, C.: Triassic tectonics of the southern margin of the South China Block. C. R.
510   Geosci., 348, 5–14, doi:10.1016/j.crte.2015.06.012, 2016.

511   Feng, Q.L., He, W.H., Gu, S.Z., Meng, Y.Y., Jin, Y.X., and Zhang, F.: Radiolarian evolution during the latest Permian in
512   South China. Global Planet. Change, 55, 177–192, doi:10.1016/j.gloplacha.2006.06.012, 2007.

513   Feng, Q.L., and Algeo, T.J.: Evolution of oceanic redox conditions during the Permo-Triassic transition: Evidence from
514   deepwater radiolarian facies. Earth-Sci. Rev., 137, 34–51, doi:10.1016/j.earscirev.2013.12.003, 2014.

515   Feng, Z.Z., Bao, Z.-D., Zheng, X.-J., and Wang, Y.: There was no "Great Bank of Guizhou" in the Early Triassic in Guizhou
516   Province, South China. J. Palaeogeogr., 4, 99–108, doi:10.3724/SP.J.1261.2015.00070, 2015.

517   Galfetti, T., Bucher, H., Ovtcharova, M., Schaltegger, U., Brayard, A., Brühwiler, T., Goudemand, N., Weissert, H.,
518   Hochuli, P.A., Cordey, F., and Guodun, K.: Timing of the Early Triassic carbon cycle perturbations inferred from
519   new U–Pb ages and ammonoid biochronozones. Earth Planet. Sc. Lett., 258, 593–604,
520   doi:10.1016/j.epsl.2007.04.023, 2007.

521   Galfetti, T., Bucher, H., Martini, R., Hochuli, P.A., Weissert, H., Crasquin-Soleau, S., Brayard A., Goudemand, N.,
522   Brühwiler, T., and Guodun, K.: Evolution of Early Triassic outer platform paleoenvironments in the Nanpanjiang
523   Basin (South China) and their significance for the biotic recovery. Sediment. Geol., 204, 36–60,
524   doi:10.1016/j.sedgeo.2007.12.008, 2008.

525   Gao, Q., Zhang, N., Xia, W., Feng, Q., Chen, Z.-Q., Zheng, J., Griffin, W.L., O'Reilly, S.Y., Pearson, N.J., Wang, G., Wu,
526   S., Zhong, W., and Sun, X.: Origin of volcanic ash beds across the Permian-Triassic boundary, Daxiakou, South
527   China: Petrology and U-Pb age, trace elements and Hf-isotope composition of zircon. Chem. Geol., 360–361, 41–53,
528   doi:10.1016/j.chemgeo.2013.09.020, 2013.

529   Golonka, J., and Ford, D.: Pangean (Late Carboniferous-Middle Jurassic) paleoenvironment and lithofacies. Palaeogeogr.
530   Palaeocl., 161, 1–34, doi:10.1016/s0031-0182(00)00115-2, 2000.

531   Guizhou Bureau of Geology and Mineral Resources: Regional geology of Guizhou Province. Geological Memoir, 1 (6), 700
532   p. (in Chinese, with English summary), scale 1:500,000, 1987.

533   Haslett, J., and Parnell, A.: A simple monotone process with application to radiocarbon-dated depth chronologies. J. Roy.
534   Stat. Soc. C-App., 57, 399–418, doi:10.1111/j.1467-9876.2008.00623.x, 2008.

535 He, W.H., Shen, S.Z., Feng, Q.L., and Gu, S.Z.: A Late Changhsingian (Late Permian) deepwater brachiopod fauna from the
536   Talung Formation at the Dongpan section, southern Guangxi, South China. J. Paleontol., 79, 927–938,
537   doi:10.1666/0022-3360(2005)079[0927:ALCLPD]2.0.CO;2, 2005.

538 He, W.H., Shi, G.R., Feng, Q.L., Campi, M.J., Gu, S.Z., Bu, J.J., Peng, Y.Q., and Meng, Y.Y.: Brachiopod miniaturization
539   and its possible causes during the Permian-Triassic crisis in deep water environments, South China. Palaeogeogr.
540   Palaeocl., 252, 145–163, doi:10.1016/j.palaeo.2006.11.040, 2007.

541 Hiess, J., Condon, D.J., McLean, N., and Noble, S.R.: $^{238}U/^{235}U$ Systematics in terrestrial uranium-bearing minerals. Science,
542   335, 1610–1614, doi:10.1126/science.1215507, 2012.

543 Hochuli, P.A., Hermann, E., Vigran, J.S., Bucher, H., and Weissert, H.: Rapid demise and recovery of plant ecosystems
544   across the end-Permian extinction event. Global Planet. Change, 74, 144–155, doi:10.1016/j.gloplacha.2010.10.004,
545   2010.

546 Jiang, H., Lai, X., Yan, C., Aldridge, R.J., Wignall, P., and Sun, Y.: Revised conodont zonation and conodont evolution
547   across the Permian-Triassic boundary at the Shangsi section, Guangyuan, Sichuan, South China. Global Planet.
548   Change, 77, 102–115, doi:10.1016/j.gloplacha.2011.04.003, 2011.

549 Jin, Y.G., Shen, S.Z., Henderson, C.M., Wang, X.D., Wang, W., Wang, Y., Cao, C.Q., and Shang, Q.H.: The Global
550   Stratotype Section and Point (GSSP) for the boundary between the Capitanian and Wuchiapingian stage (Permian).
551   Episodes, 29, 253–262, 2006.

552 Kuiper, K.F., Deino, A., Hilgen, F.J., Krijgsman, W., Renne, P.R., and Wijbrans, J.R.: Synchronizing Rock Clocks of Earth
553   History. Science, 320, 500–504, doi:10.1126/science.1154339, 2008.

554 Lehrmann, DJ., Payne, J.L., Felix, S.V., Dillett, P.M., Wang, H., Yu, Y., and Wei, J.: Permian-Triassic Boundary Sections
555   from Shallow-Marine Carbonate Platforms of the Nanpanjiang Basin, South China: Implications for Oceanic
556   Conditions Associated with the End-Permian Extinction and Its Aftermath. Palaios, 18, 138–152, doi:10.1669/0883-
557   1351(2003)18<138:pbsfsc>2.0.co;2, 2003.

558 Lehrmann, D.J., Pei, D., Enos, P., Ellwood, B.B., Zhang, J., Wei, J., Dillett, P., Koenig, J., Steffen, K., Druke, D., Gross, J.,
559   Kessel, B., and Newkirk, T.: Impact of differential tectonic subsidence on isolated carbonate platform evolution:
560   Triassic of the Nanpanjiang basin, south China. Am. Assoc. Petr. Geol. B., 91, 287–320, doi:10.1306/10160606065,
561   2007.

562 Lehrmann, D.J., Stepchinski, L., Altiner, D., Orchard, M.J., Montgomery, P., Enos, P., Ellwood, B.B., Bowring, S.A.,
563   Ramezani, J., Wang, H., Wei, J., Yu, M., Griffiths, J.D., Minzo, M., Schaall, E.K., Lil, X., Meyerl, K.M., and Payne,
564   J.L.: An integrated biostratigraphy (conodonts and foraminifers) and chronostratigraphy (paleomagnetic reversals,
565   magnetic susceptibility, elemental chemistry, carbon isotopes and geochronology) for the Permian-Upper Triassic
566   strata of Guandao section, Nanpanjiang Basin, south China. J. Asian Earth Sci., 108, 117–135,
567   doi:10.1016/j.jseaes.2015.04.030, 2015.

568 Luo, G.M., Lai, X.L., Feng, Q.L., Jiang, H.S., Wignall, P., Zhang, K.X., Sun, Y.D., and Wu, J.: End-Permian conodont fauna
569  from Dongpan section: Correlation between the deep- and shallow-water facies. Sci. China Ser. D, 51, 1611–1622,
570  doi:10.1007/s11430-008-0125-1, 2008.

571 Luo, G.M., Wang, Y., Yang, H., Algeo, T.J., Kump, L.R., Huang, J., and Xie, S.C.: Stepwise and large-magnitude negative
572  shift in $\delta^{13}C_{carb}$ preceded the main marine mass extinction of the Permian-Triassic crisis interval. Palaeogeogr.
573  Palaeocl., 299, 70–82, doi:10.1016/j.palaeo.2010.10.035, 2011.

574 Mattinson, J.M.: Zircon U-Pb chemical abrasion ("CA-TIMS") method: combined annealing and multi-step partial
575  dissolution analysis for improved precision and accuracy of zircon ages. Chem. Geol., 220, 47–66,
576  doi:10.1016/j.chemgeo.2005.03.011, 2005.

577 McLean, N.M., Bowring, J.F., and Bowring, S.A.: An algorithm for U-Pb isotope dilution data reduction and uncertainty
578  propagation. Geochem. Geophys. Geosyst., 12, 6, doi:10.1029/2010gc003478, 2011.

579 Meng, Y.Y., Zhou, Q., and Li, Y.K.: The characteristics and controlling sedimentary facies and granitoid analysis of the
580  middle part of Pingxing-Dongmeng large fault. Guangxi Geology, 15, 1–4 (in Chinese), 2002.

581 Mundil, R., Metcalfe, I., Ludwig, K.R., Renne, P.R., Oberli, F., and Nicoll, R.S.: Timing of the Permian-Triassic biotic
582  crisis: Implications from new zircon U/Pb age data (and their limitations). Earth Planet. Sc. Lett., 187, 131–145,
583  doi:10.1016/s0012-821x(01)00274-6, 2001.

584 Mundil, R., Ludwig, K.R., Metcalfe, I., and Renne, P.R.: Age and Timing of the Permian Mass Extinctions: U/Pb Dating of
585  Closed-System Zircons. Science, 305, 1760–1763, doi:10.1126/science.1101012, 2004.

586 Ovtcharova, M., Bucher, H., Schaltegger, U., Galfetti, T., Brayard, A., and Guex, J.: New Early to Middle Triassic U-Pb
587  ages from South China: calibration with ammonoid biochronozones and implications for the timing of the Triassic
588  biotic recovery. Earth Planet. Sc. Lett., 243, 463–475, doi:10.1016/j.epsl.2006.01.042, 2006.

589 Ovtcharova, M., Goudemand, N., Hammer, O., Guodun, K., Cordey, F., Galfetti, T., Schaltegger, U., and Bucher, H.:
590  Developing a strategy for accurate definition of a geological boundary through radio-isotopic and biochronological
591  dating: The Early–Middle Triassic boundary (South China). Earth-Sci. Rev., 146, 65–76,
592  doi:10.1016/j.earscirev.2015.03.006, 2015.

593 Parnell, A.C., Haslett, J., Allen, J.R.M., Buck, C.E., and Huntley, B.: A flexible approach to assessing synchroneity of past
594  events using Bayesian reconstructions of sedimentation history. Quat. Sci. Rev., 27, 1872–1885,
595  doi:10.1016/j.quascirev.2008.07.009, 2008.

596 Parnell, A.C., Buck, C.E., and Doan, T.K.: A review of statistical chronology models for high-resolution, proxy-based
597  Holocene palaeoenvironmental reconstruction. Quat. Sci. Rev., 30, 2948–2960, doi:10.1016/j.quascirev.2011.07.024,
598  2011.

599 Payne, J.L., Turchyn, A.V., Paytan, A., DePaolo, D.J., Lehrmann, D.J., Yu, M.Y., and Wei, J.Y.: Calcium isotope
600  constraints on the end-Permian mass extinction. P. Natl. Acad. Sci. USA, 107, 8543–8548,
601  doi:10.1073/pnas.0914065107, 2010.

602 Raup, D.M: Size of the Permo-Triassic bottleneck and its evolutionary implications. Science, 206, 217–218,
603   doi:10.1126/science.206.4415.217, 1979.

604 Renne, P.R., Black, M.T., Zichao, Z., Richards, M.A., and Basu, A.R.: Synchrony and causal relations between Permian-
605   Triassic Boundary crises and Siberian flood volcanism. Science, 269, 1413–1416,
606   doi:10.1126/science.269.5229.1413, 1995.

607 Retallack, G.J., and Jahren, A.H.: Methane release from igneous intrusion of coal during Late Permian extinction events. J.
608   Geol., 116, 1–20, doi:10.1086/524120, 2008.

609 Samperton, K.M., Schoene, B., Cottle, J.M., Keller, C.B., Crowley, J.L., and Schmitz, M.D.: Magma emplacement,
610   differentiation and cooling in the middle crust: Integrated zircon geochronological-geochemical constraints from the
611   Bergell Intrusion, Central Alps. Chem. Geol., 417, 322–340, doi:10.1016/j.chemgeo.2015.10.024, 2015.

612 Schoene, B., Crowley, J.L., Condon, D.J., Schmitz, M.D., and Bowring, S.A.: Reassessing the uranium decay constants for
613   geochronology using ID-TIMS U-Pb data. Geochim. Cosmochim. Ac., 70, 426–445, doi:10.1016/j.gca.2005.09.007,
614   2006.

615 Shang, Q.H., Vachard, D., and Caridroit, M.: Smaller foraminifera from the Late Changhsingian (Latest Permian) of
616   Southern Guangxi and discussion on the Permian-Triassic boundary. Acta Micropalaeontologica Sinica, 20, 377–388,
617   2003.

618 Shen, S.Z., Wang, Y., Henderson, C.M., Cao, C.Q., and Wang, W.: Biostratigraphy and lithofacies of the Permian System in
619   the Laibin-Heshan area of Guangxi, South China. Palaeoworld, 16, 120–139, doi:10.1016/j.palwor.2007.05.005,
620   2007.

621 Shen, S.Z., Crowley, J.L., Wang, Y., Bowring, S.A., Erwin, D.H., Sadler, P.M., Cao, C.Q., Rothman, D.H., Henderson,
622   C.M., Ramezani, J., Zhang, H., Shen, Y., Wang, X.D., Wang, W., Mu, L., Li, W.Z., Tang, Y.G., Liu, X.L., Liu, L.J.,
623   Zeng, Y., Jiang, Y.F., and Jin, Y.G.: Calibrating the end-Permian mass extinction. Science, 334, 1367–1372,
624   doi:10.1126/science.1213454, 2011.

625 Shen, J., Algeo, T.J., Zhou, L., Feng, Q., Yu, J., and Ellwood, B.: Volcanic perturbations of the marine environment in South
626   China preceding the latest Permian mass extinction and their biotic effects. Geobiology, 10, 82–103,
627   doi:10.1111/j.1472-4669.2011.00306.x, 2012.

628 Shen, J., Algeo, T.J., Hu, Q., Xu, G.Z., Zhou, L., and Feng, Q.L.: Volcanism in South China during the Late Permian and its
629   relationship to marine ecosystem and environmental changes. Global Planet. Change, 105, 121–134,
630   doi:10.1016/j.gloplacha.2012.02.011, 2013a.

631 Shen, S.Z., Cao, C.Q., Zhang, H., Bowring, S.A., Henderson, C.M., Payne, J.L., Davydov, V.I., Chen, B., Yuan, D.X.,
632   Zhang, Y.C., Wang, W., and Zheng, Q.F.: High-resolution $\delta^{13}C_{carb}$ chemostratigraphy from latest Guadalupian
633   through earliest Triassic in South China and Iran. Earth Planet. Sc. Lett., 375, 156–165,
634   doi:10.1016/j.epsl.2013.05.020, 2013b.

635 Stanley, S.M., and Yang, X.: A double mass extinction at the end of the Paleozoic era. Science, 266, 1340–1344,
636   doi:10.1126/science.266.5189.1340, 1994.

637 Svensen, H., Planke, S., Polozov, A.G., Schmidbauer, N., Corfu, F., Podladchikov, Y.Y., and Jamtveit, B.: Siberian gas
638   venting and the end-Permian environmental crisis. Earth Planet. Sc. Lett., 277, 490–500,
639   doi:10.1016/j.epsl.2008.11.015, 2009.

640 Van Valen, L.: A resetting of Phanerozoic community evolution. Nature, 307, 50–52, doi:10.1038/307050a0, 1984.

641 Wang, Y., and Jin, Y.: Permian palaeogeographic evolution of the Jiangnan Basin, South China. Palaeogeogr. Palaeocl., 160,
642   35–44, doi:10.1016/s0031-0182(00)00043-2, 2000.

643 Winguth, C., and Winguth, A.M.E.: Simulating Permian-Triassic oceanic anoxia distribution: implications for species
644   extinction and recovery. Geology, 40, 127–130, doi:10.1130/g32453.1, 2012.

645 Wu, J., Feng, Q.L., Gui, B.W., and Liu, G.C.: Some new radiolarian species and genus from Upper Permian in Guangxi
646   Province, South China. J. Paleontol. 84, 879–894, doi:10.1666/09-057.1, 2010.

647 Xia, W.C., Zhang, N., Wang, G.Q., and Kakuwa, Y.: Pelagic radiolarian and conodont biozonation in the Permo-Triassic
648   boundary interval and correlation to the Meishan GSSP. Micropaleontology, 50, 27–44, doi:10.1661/0026-
649   2803(2004)050[0027:pracbi]2.0.co;2, 2004.

650 Yin, H.F.: Bivalves near the Permian-Triassic boundary in South China. J. Paleontol., 59, 572–600, 1985.

651 Yin, H.F., Zhang, K.X., Tong, J.N., Yang, Z.Y., and Wu, S.B.: The global stratotype section and point (GSSP) of the
652   Permian-Triassic boundary. Episodes, 24, 102–114, 2001.

653 Yin, H.F., Feng, Q.L., Lai, X.L., Baud, A., and Tong, J.N.: The protracted Permo-Triassic crisis and multi-episode extinction
654   around the Permian-Triassic boundary. Global Planet. Change, 55, 1–20, doi:10.1016/j.gloplacha.2006.06.005, 2007.

655 Yin, H.F., Jiang, H.S., Xia, W.C. Feng, Q., Zhang, N., and Shen, J.: The end-Permian regression in South China and its
656   implication on mass extinction. Earth-Sci. Rev., 137, 19–33, doi:10.1016/j.earscirev.2013.06.003, 2014.

657 Yuan, A., Crasquin-Soleau, S., Feng, Q.L., and Gu, S.Z.: Latest Permian deep-water ostracods from southwestern Guangxi,
658   South China. J. Micropalaeontol., 26, 169–191, doi:10.1144/jm.26.2.169, 2007.

659 Yuan, D., Shen, S., Henderson, C.M., Chen, J., Zhang, H., and Feng, H.: Revised conodont-based integrated high-resolution
660   timescale for the Changhsingian Stage and end-Permian extinction interval at the Meishan sections, South China.
661   Lithos, 204, 220–245, doi:10.1016/j.lithos.2014.03.026, 2015.

662 Zhang, F., Feng, Q.L., He, W.H., Meng, Y.Y., and Gu, S.Z.: Multidisciplinary stratigraphy across the Permian-Triassic
663   boundary in deep-water environment of Dongpan section, south China. Norw. J. Geol., 86, 125–131, 2006.

664 Zhao, J.K., Liang, X.l., and Zheng, Z.G.: Late Permian Cephalopods in South China. Science Press, Beijing (in Chinese),
665   1978.

666 Ziegler, A.M., Hulver, M.L., and Rowley, D.B.: Permian World Topography and Climate. In: Martini, I.P. (Ed.) Late glacial
667   and postglacial environmental changes: Quaternary, Carboniferous-Permian, and Proterozoic. New York, USA,
668   Oxford University Press, 343 p., 1997.
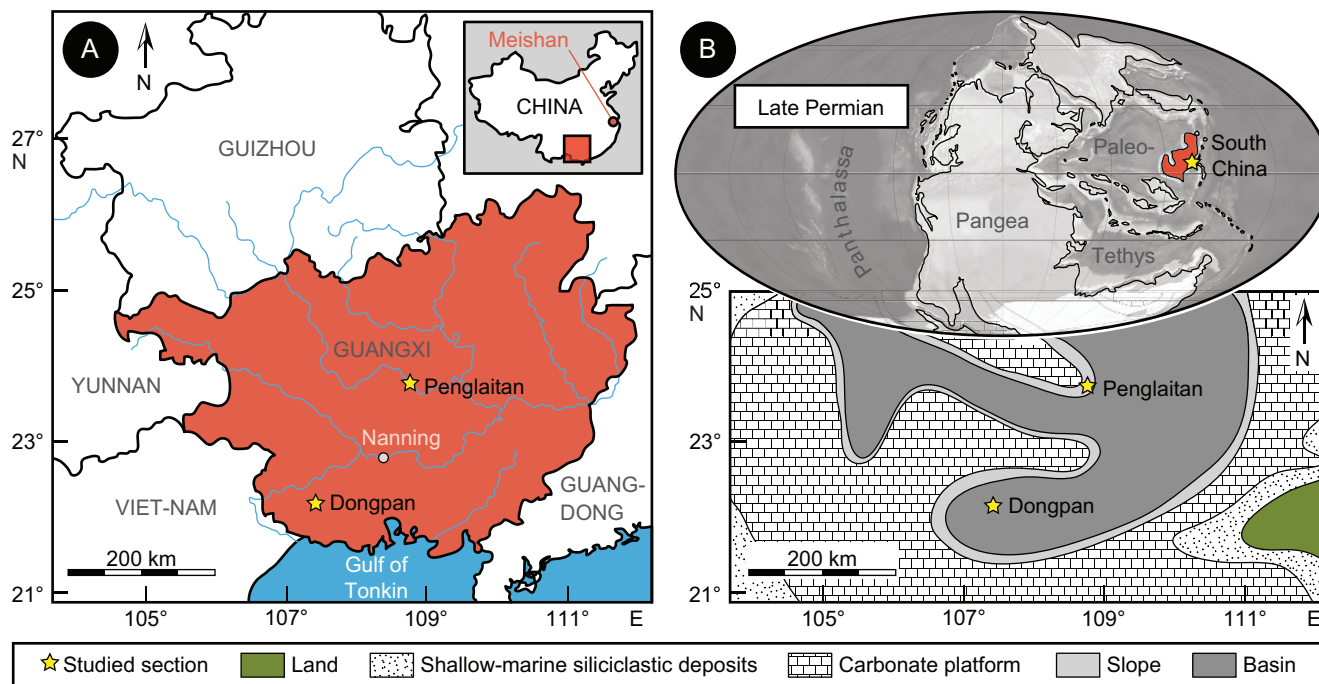
Fig. 1. A) Locality map showing the position of the studied sections in the Guangxi province, China. B) Late Permian paleogeographic reconstruction after Ziegler et al. (1997), showing the location of the South China Block in the peri-Gondwana region. Beneath the paleogeographic map of the Nanpanjiang Basin in South China indicating the position of the Dongpan and Penglaitan section during Late Permian times (base map modified after Wang and Jin, 2000).
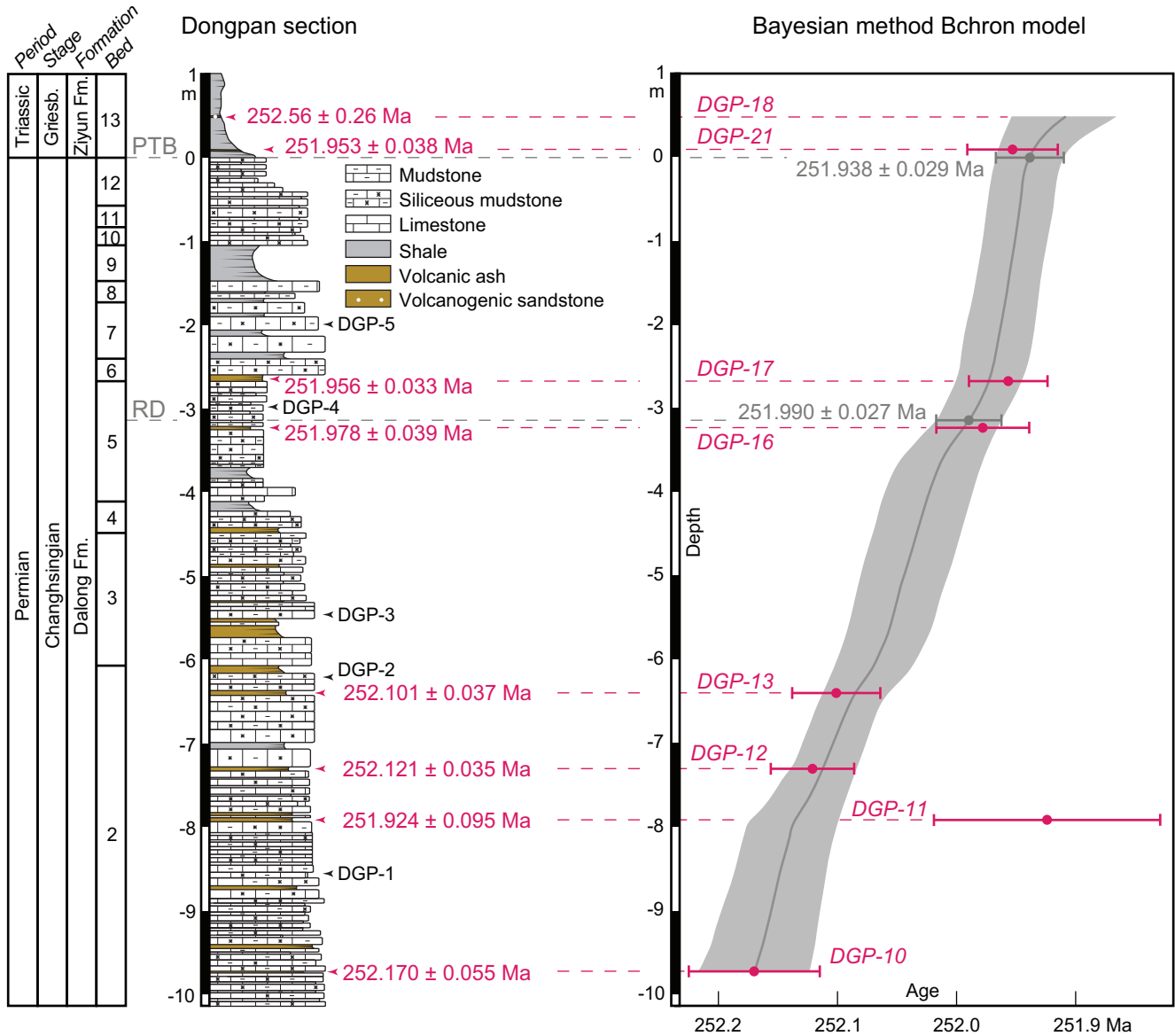
Fig. 2. Stratigraphy and geochronology for the Dongpan section from late Changhsingian to Griesbachian showing weighted mean $^{206}Pb/^{238}U$ dates of the volcanic ash beds and volcanogenic sandstones. U-Pb data of DGP-21 is taken from Baresel et al. (in press). Investigated radiolarian samples (DGP-1 to DGP-5) are shown in their stratigraphic positions. The Bayesian Bchron age-depth model is presented with its median (middle grey line) and its associated 95 % confidence interval (grey area). Radioisotopic dates together with their uncertainty (red horizontal bars) are presented as $^{206}Pb/^{238}U$ weighted mean dates of the dated volcanic ash beds in their stratigraphic positions. Predicted dates for the onset of the radiolarian decline (RD) and the Permian-Triassic Boundary (PTB) are calculated with their associated uncertainty using the Bayesian Bchron age-depth model assuming stratigraphic superposition.

683
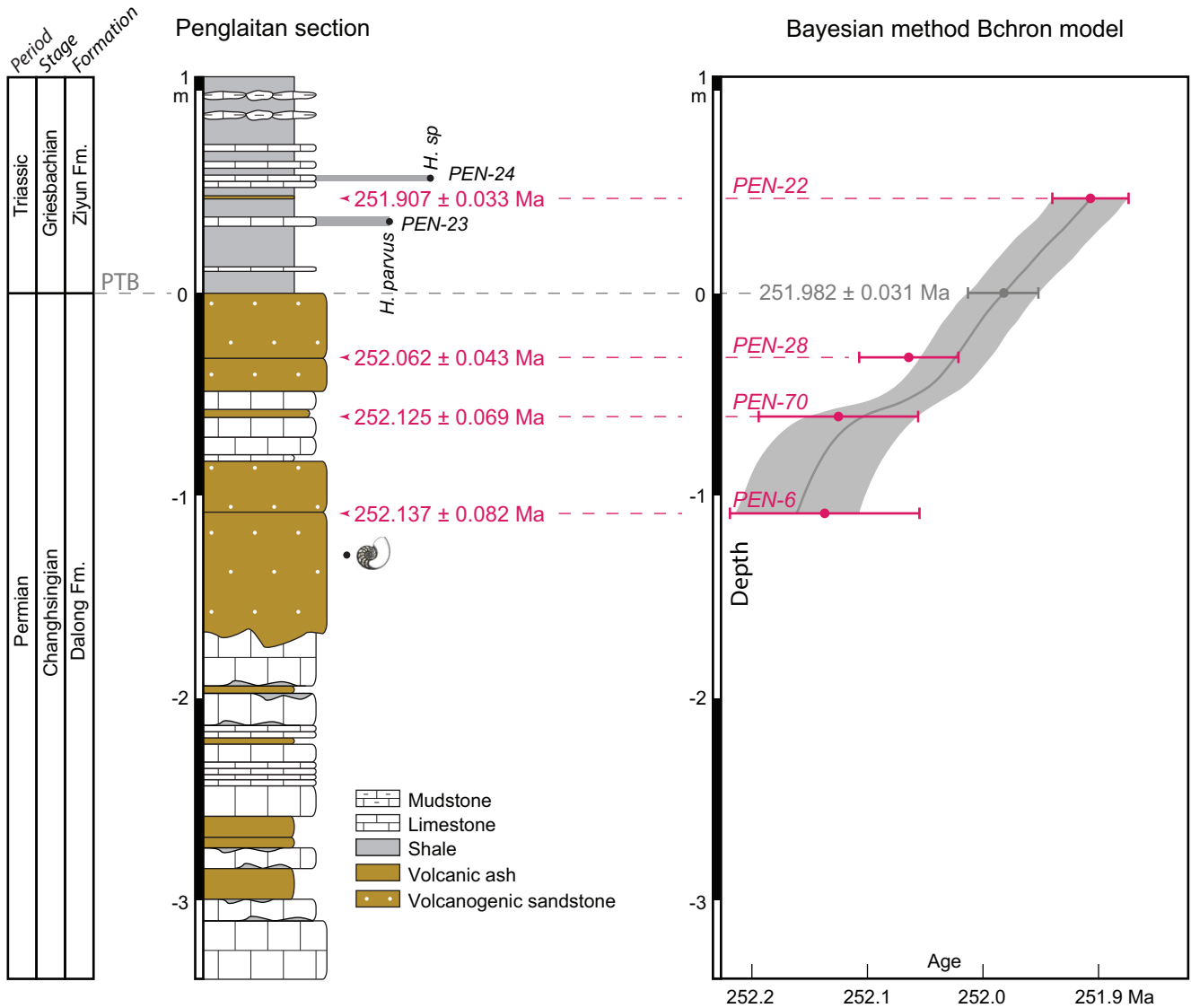
Fig. 3. Stratigraphy and geochronology for the Penglaitan section from late Changhsingian to Griesbachian showing weighted mean ^{206}Pb/^{238}U dates of the volcanic ash beds and volcanogenic sandstones. U-Pb data of PEN-28 and PEN-22 are taken from Baresel et al. (in press). Investigated conodont samples (PEN-23 and PEN-24) and first occurrence of Triassic conodonts are shown in their stratigraphic positions. A poorly preserved Permian nautiloid is indicated in its stratigraphic position ca. 1.3 m below the Permian-Triassic Boundary (PTB). The Bayesian Bchron age-depth model is presented with its median (middle grey line) and its associated 95 % confidence interval (grey area). Radioisotopic dates together with their uncertainty (red horizontal bars) are presented as ^{206}Pb/^{238}U weighted mean dates of the dated volcanic ash beds in their stratigraphic positions. Predicted dates for the PTB are calculated with their associated uncertainty using the Bayesian Bchron age-depth model assuming stratigraphic superposition.

693
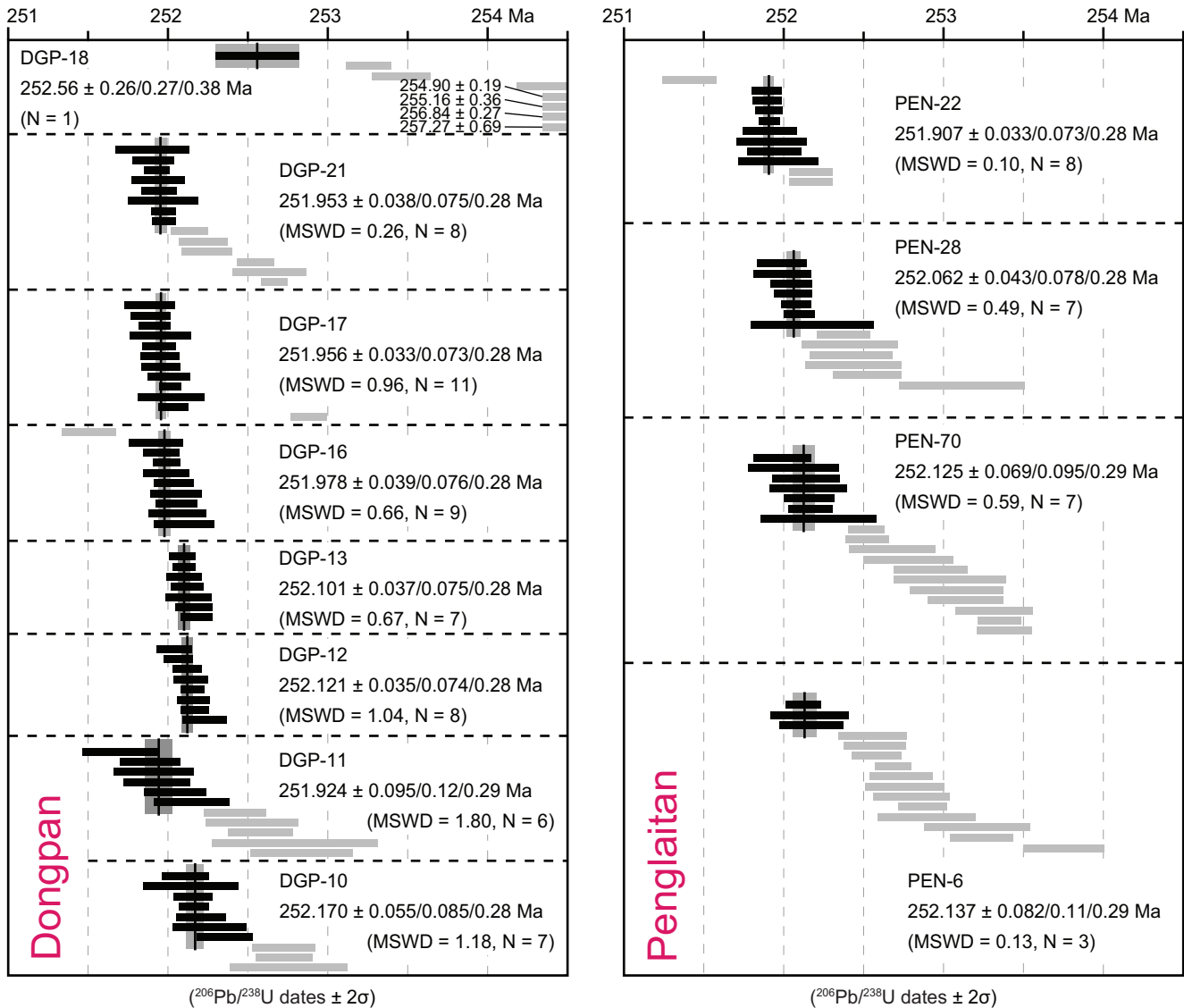
Fig. 4. Single-grain zircon analysis and ²⁰⁶Pb/²³⁸U weighted mean dates for Dongpan and Penglaitan volcanic ash beds and volcanogenic sandstones. U-Pb data of DGP-21, PEN-28 and PEN-22 are taken from Baresel et al. (in press). Each horizontal bar represents a single zircon grain analysis including its 2σ analytical (internal) uncertainty whereas grey bars are not included in the weighted mean calculation. Vertical lines represent the weighted mean age, with the associated 2σ uncertainty (in grey). Uncertainty of the weighted mean dates is reported as 2σ internal, 2σ external uncertainty including tracer calibration and 2σ external uncertainty including ²³⁸U decay constant uncertainty; MSWD - mean square of weighted deviates.
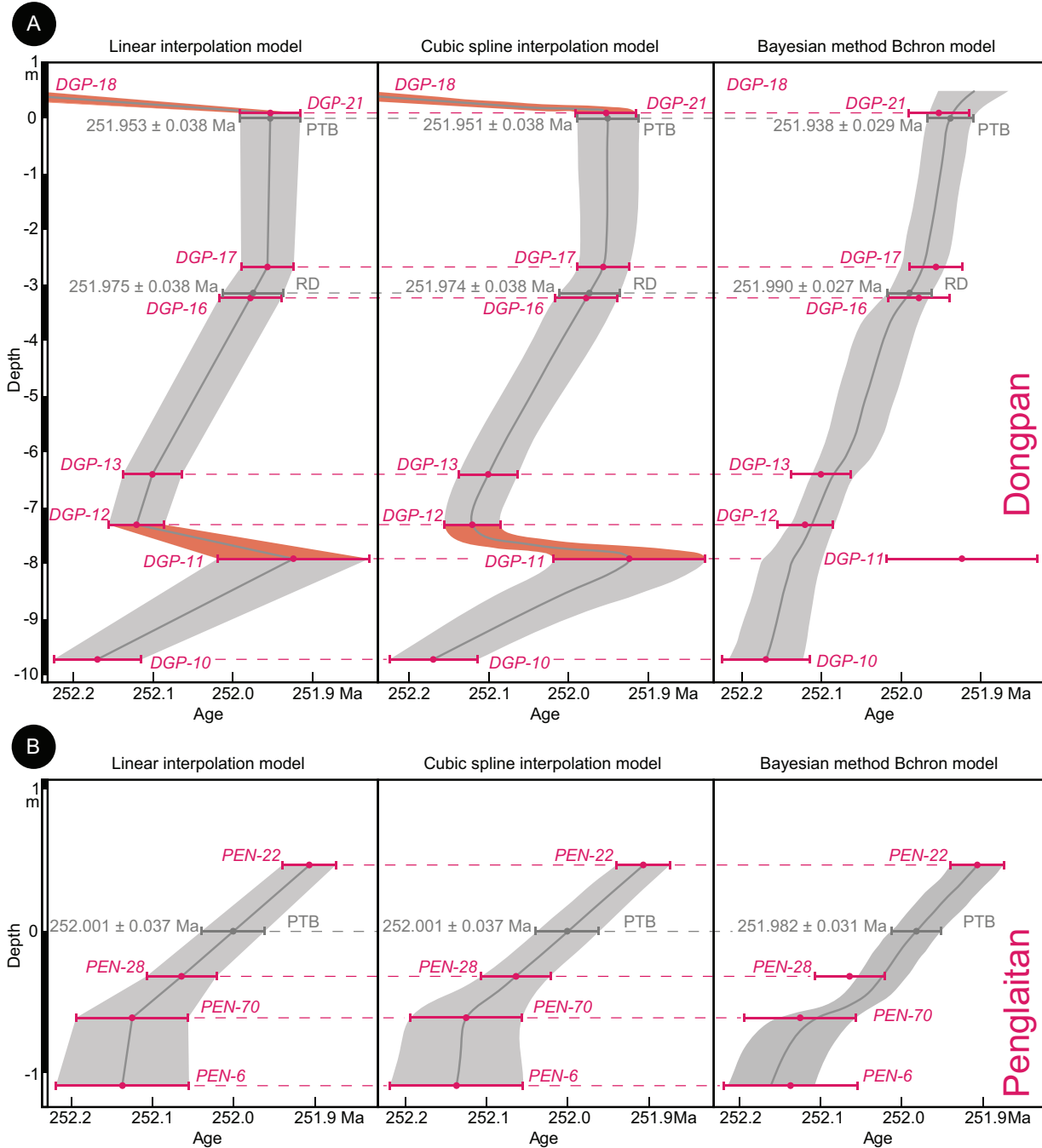
Fig. 5. Comparison of the different age-depth-models based on linear interpolation, cubic spline fit and Bayesian statistics for A) Dongpan and B) Penglaitan. Each age-depth model is presented with its median (middle grey line) and its associated 95 % confidence interval (grey area). Radioisotopic dates, used in the age-depth-models, together with their uncertainty (red horizontal bars) are presented as $^{206}Pb/^{238}U$ weighted mean dates of the Dongpan and Penglaitan volcanic ash beds and volcanogenic sandstones in their stratigraphic positions. U-Pb data of DGP-21, PEN-28 and PEN-22 are taken from Baresel et al. (in press). Predicted dates (grey horizontal bars) for the onset of the radiolarian decline (RD) and the Permian-Triassic Boundary (PTB) in Dongpan and Penglaitan are calculated with their associated uncertainty using the different age-depth models.

708
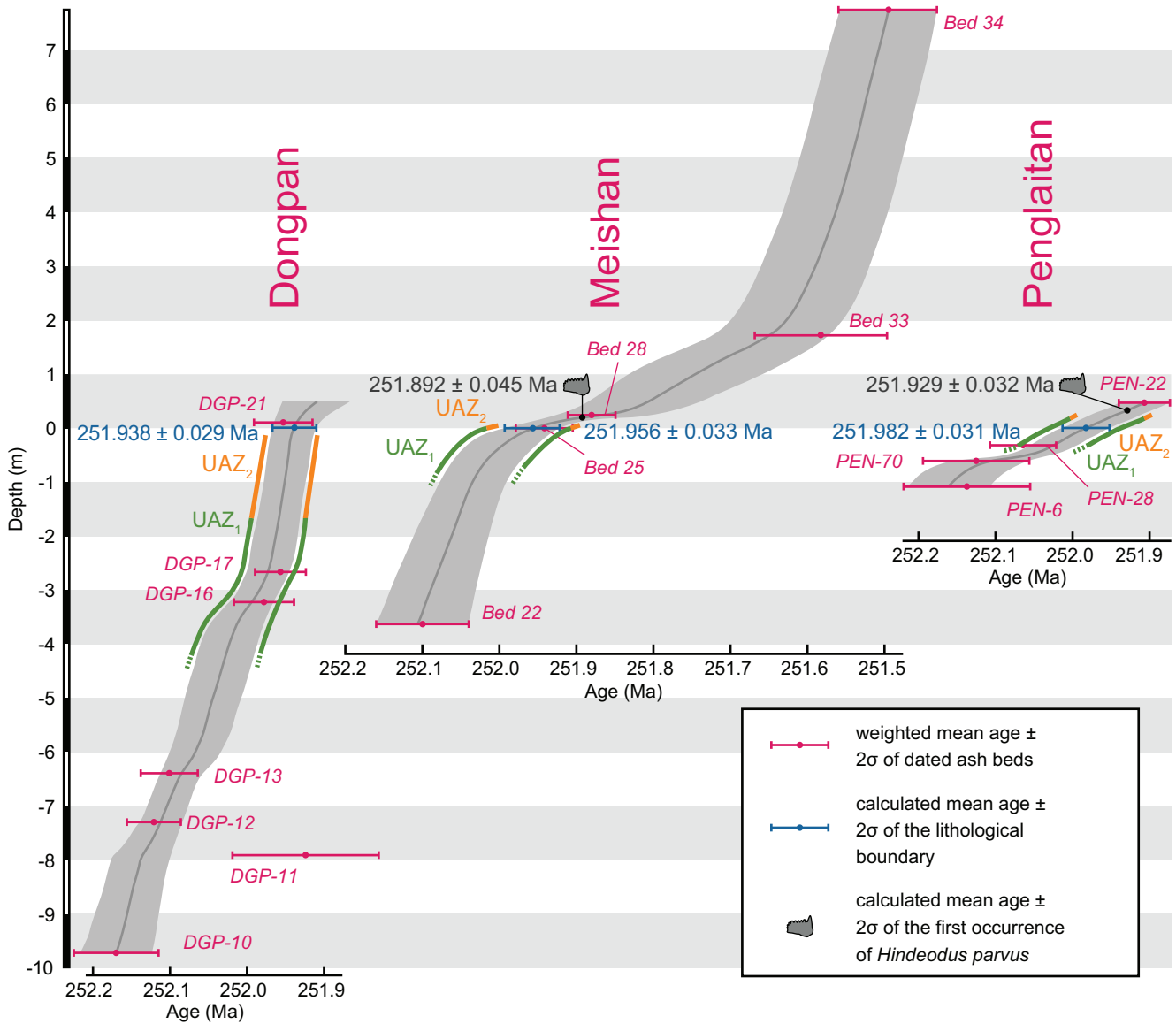
Fig. 6. Comparison of Bayesian Bchron age models for Dongpan, Penglaitan and the GSSP section Meishan D. Predicted dates together with their uncertainty for the lithological boundaries and the first occurrence of the conodont *Hindeodus parvus* at Dongpan and Penglaitan are calculated using U-Pb ages of this study and of Baresel et al. (in press), and the U-Pb ages of Burgess et al. (2014) for Meishan. The durations of the conodont UAZ1 and UAZ2 (Brosse et al., 2016) are inferred from the Bchron age model of Meishan and projected to the model of Dongpan and Penglaitan, respectively.
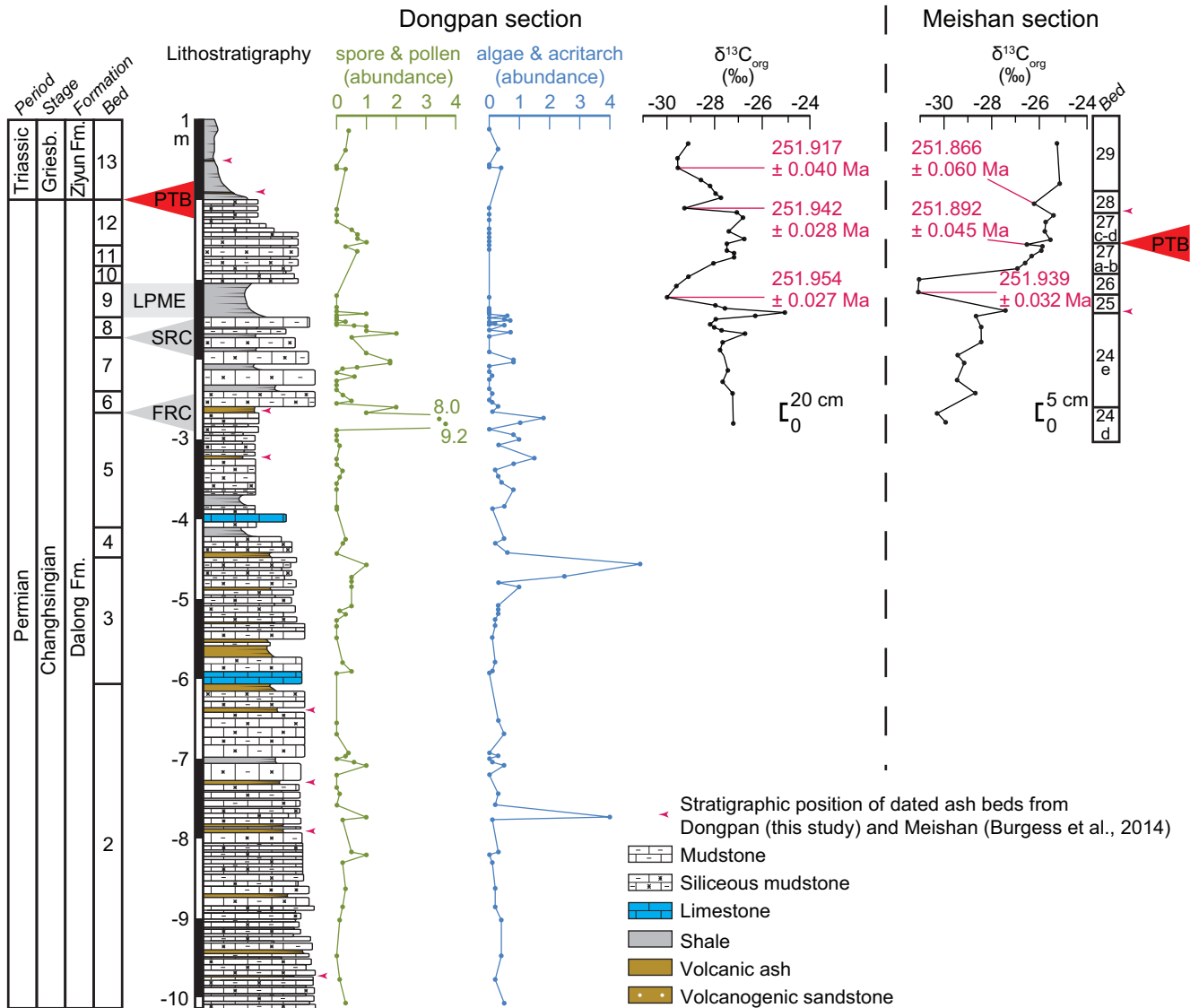
Fig. 7. Comparison of the organic carbon isotope chemostratigraphy of Dongpan (Zhang et al., 2006) with that of Meishan (Cao et al., 2002). Dates and their associated uncertainty for the negative carbon isotope excursions in both sections are revealed from the Bayesian Bchron age models of Dongpan and Meishan, respectively. Abundance of spores and pollen, as well as algae and acritarchs (i.e. spores/100 cm³ of soil) in Dongpan are from Shen et al. (2012). Stratigraphic positions of the First Radiolarian Crisis (FRC) and Second Radiolarian Crisis (SRC) (after Feng et al., 2007), the Latest Permian Extinction Event (LPME) in Dongpan and the Permian-Triassic Boundary (PTB) in both sections are indicated as well. Meishan section thickness is not to scale with Dongpan section.

Appendix A: Samples

The Dongpan section is situated at 22°16'11.80"N and 107°41'31.30"E, north-east of Liuqiao. The Penglaitan section is situated at 23°41'8.4"N and 109°18'21.0"E, east of Laibin.
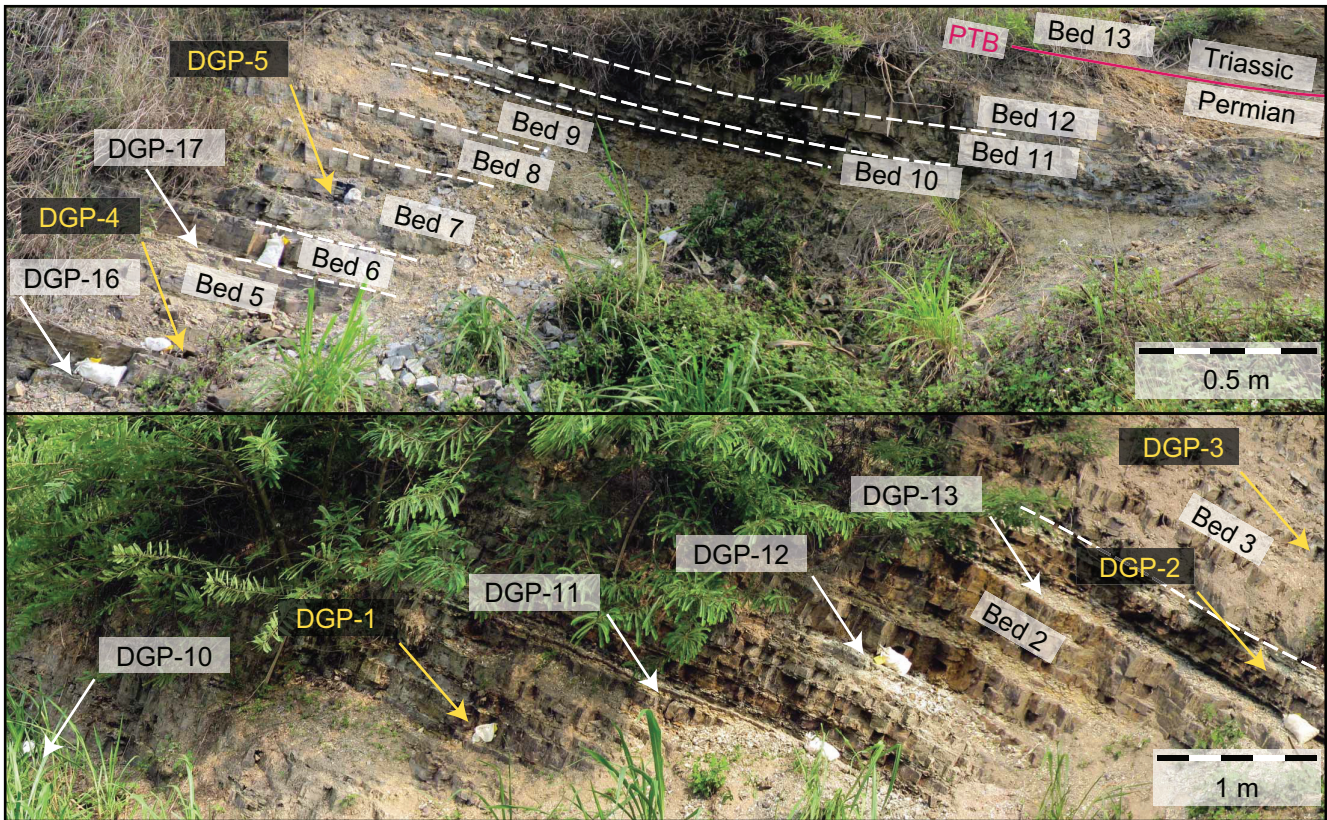
Fig. A1. Studied volcanic ash beds (in black), radiolarian samples (in yellow), and their associated beds of the Changhsingian Dalong Fm. at the Dongpan section. Both pictures present the continuous Dongpan section, where the upper picture is stratigraphically above the lower one. The Permian-Triassic boundary (PTB) in Dongpan is marked by the lithological boundary between the Upper Permian Dalong Fm. and the Lower Triassic Ziyun Fm.

734
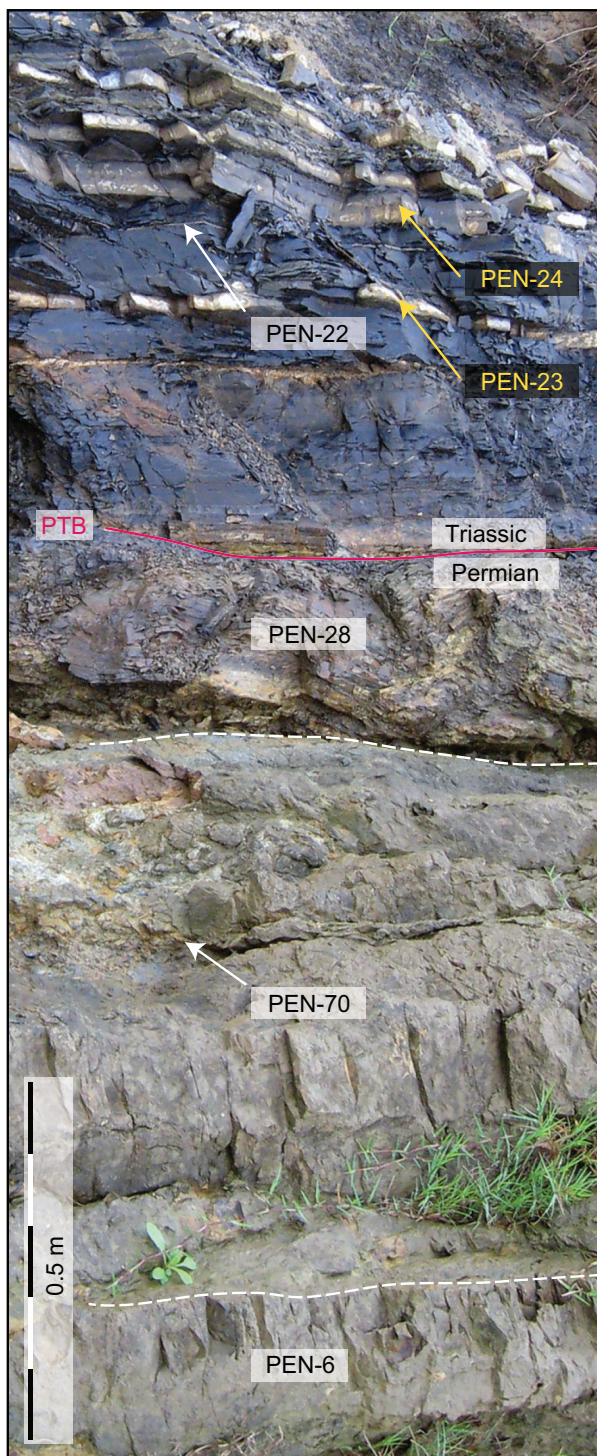
Fig. A2. Studied volcanic ash beds and volcaniclastic sandstones (in black), and conodont samples (in yellow) of the Penglaitan
735
section. The Permian-Triassic boundary (PTB) is marked by the lithological boundary between the Upper Permian Dalong Fm.
736
and the Lower Triassic Ziyun Fm.
737

Appendix B: U-Pb Zircon CA-ID-TIMS analysis

The samples were crushed and milled, and the powder was wet-sieved to remove the clay fraction. Heavy minerals were isolated using methylene iodide. Single zircons were microscopically inspected and euhedral crystals were picked for annealing at 900°C for ~48 h, followed by chemical abrasion with 40 % HF and trace HNO_3 in pressurized 200 µl Savillex mini-capsules at 180°C for 18 h to minimize Pb loss effects (Mattinson, 2005). Since Ovtcharova et al. (2015) still revealed apparent Pb loss in some zircon grains after 15 h of chemical abrasion, this study was optimized to the longer duration of 18 h to effectively overcome this obstacle.

After several washing steps with water, 6 N HCl, and 3 N HNO_3, single crystals were loaded in 200 µl Savillex capsules, spiked with ~4 mg of the EARTHTIME ^{202}Pb-^{205}Pb-^{233}U-^{235}U tracer solution (hereafter referred to as ET2535; Condon et al., 2015) and dissolved in ~70 µl 40 % HF and trace HNO_3 at 210°C for 48 h. After dissolution, samples were dried and re-dissolved in 6 N HCl at 180°C for 12 h, dried down again and re-dissolved in 3 N HCl. U and Pb were collected in 3 ml Savillex beakers after separation in a modified single 50 µl column anion exchange chemistry (Krogh, 1973) and dried down with a drop of 0.05 M H_3PO_4. They were loaded on a single outgassed Re filament with a Si-gel emitter modified from Gerstenberger and Haase (1997). Measurements of U and Pb isotopes were performed on a Thermo TRITON thermal ionization mass spectrometer utilizing the ET2535 tracer calibration version 3.0 defined by Condon et al. (2015). Pb isotopes were measured in dynamic mode on a MasCom secondary electron multiplier with a deadtime of 23 ns. Instrumental mass fractionation was corrected using the fractionation factor derived from the measured $^{202}Pb/^{205}Pb$ ratio relative to a true value of 0.99924. $BaPO_2$ interferences on mass 202 to 205 were corrected by determining $^{138}Ba^{31}P^{16}O^{16}O$ concentration on mass 201 assuming natural abundance of ^{138}Ba of 71.7 %. No correction was applied for isobaric interference of Tl on mass 205 (natural abundance of ^{205}Tl = 70.48 %, ^{203}Tl = 29.52 %) since routine check of the Re filaments yielded negligible concentrations on mass 203. U isotopes were measured in static mode on Faraday cups equipped with 10^{12} Ω resistors as UO_2^+ and measured ratios were corrected for isobaric interferences of $^{233}U^{18}O^{16}O$ on $^{235}U^{16}O^{16}O$ using $^{18}O/^{16}O$ of 0.0020, measured on large U500 loads, and for mass fractionation using the measured $^{233}U/^{235}U$ ratio relative to a value of 0.99506, assuming a sample $^{238}U/^{235}U$ ratio of 137.818 ± 0.045 (2σ; Hiess et al., 2012). Raw data were statistical filtered by using the Tripoli program, followed by data reduction including correct uncertainty propagation and online data visualization using U-Pb_Redux software (Bowring et al., 2011; McLean et al., 2011). U-Pb ratios and dates were calculated relative to a tracer $^{235}U/^{205}Pb$ ratio of 100.23 ± 0.046 % (2σ; Condon et al., 2015). All common Pb in the analyses was assumed to be procedural blank yielding a long-term average $^{206}Pb/^{204}Pb$ ratio of 18.469 ± 0.458, $^{207}Pb/^{204}Pb$ ratio of 15.471 ± 0.320, $^{208}Pb/^{204}Pb$ ratio of 38.011 ± 0.484 (uncertainties are given as 2σ) and an average of 0.52 pg during the course of this study.

771 **Tab. B1. U-Pb single grain zircon dates and isotopic data.**

| Fraction and sample | Dates (Ma) | | | | | Composition | | | | Isotopic Ratios | | | | | |
	206Pb/238U *a°°	±2σ (absolute)	207Pb/235U *a	±2σ (absolute)	Disc. (%) *b	Th/U *c	Pb (pg) *d	Pbc (pg) *e	206Pb/204Pb *f	206Pb/238U *g	±2σ (%)	207Pb/235U *g	±2σ (%)	207Pb/206Pb *g	±2σ (%)
Dongpan-18															
DGP 18.1	253.253	0.142	253.517	0.994	1.38	0.63	20.12	0.74	1618	0.0401	0.06	0.2836	0.44	0.0514	0.43
DGP 18.2	254.900	0.186	254.789	1.518	-0.10	0.59	11.39	0.66	1036	0.0403	0.07	0.2852	0.67	0.0513	0.66
DGP 18.3	257.274	0.689	257.017	2.366	-0.70	0.69	6.29	0.50	750	0.0407	0.27	0.2880	1.04	0.0513	0.99
DGP 18.4	255.159	0.364	254.345	2.676	-3.01	0.62	5.09	0.50	619	0.0404	0.15	0.2847	1.19	0.0512	1.16
DGP 18.5	254.752	0.568	253.430	1.742	-5.24	0.64	8.27	0.48	1025	0.0403	0.23	0.2835	0.78	0.0510	0.72
DGP 18.6	252.559	0.261	252.422	0.560	-0.22	0.64	35.48	0.51	4061	0.0399	0.11	0.2822	0.25	0.0513	0.21
DGP 18.7	256.837	0.275	256.141	2.378	-2.48	0.61	4.78	0.43	677	0.0406	0.11	0.2869	1.05	0.0512	1.03
DGP 18.8	253.456	0.184	253.776	1.592	1.61	0.58	13.80	0.86	973	0.0401	0.07	0.2839	0.71	0.0514	0.71
Dongpan-21															
DGP 21.2	252.677	0.241	252.499	0.494	-0.38	0.59	52.48	0.51	6089	0.0400	0.10	0.2823	0.22	0.0513	0.18
DGP 21.4	252.715	0.084	252.668	0.412	0.15	0.55	42.44	0.52	4883	0.0400	0.03	0.2825	0.18	0.0513	0.17
DGP 21.5	252.265	0.163	252.503	0.442	1.25	0.95	29.07	0.38	4114	0.0399	0.07	0.2823	0.20	0.0513	0.18
DGP 21.6	252.586	0.117	252.523	0.339	0.07	0.69	43.39	0.44	5721	0.0399	0.05	0.2824	0.15	0.0513	0.13
DGP 21.8	251.908	0.134	251.934	0.875	0.45	0.61	19.59	0.57	2053	0.0398	0.05	0.2816	0.39	0.0513	0.39
DGP 21.10	252.145	0.120	252.108	0.438	0.19	0.62	29.98	0.41	4356	0.0399	0.05	0.2818	0.20	0.0513	0.18
DGP 21.12	251.969	0.229	251.711	0.720	-0.73	0.67	26.37	0.46	3340	0.0398	0.09	0.2813	0.32	0.0512	0.25
DGP 21.13	251.975	0.077	252.032	0.715	0.58	0.52	17.62	0.49	2206	0.0398	0.03	0.2817	0.32	0.0513	0.33
DGP 21.14	252.240	0.157	252.369	0.850	0.84	0.77	13.19	0.40	1877	0.0399	0.06	0.2822	0.38	0.0513	0.37
DGP 21.15	251.929	0.080	251.955	0.694	0.46	0.53	19.68	0.54	2197	0.0398	0.03	0.2816	0.31	0.0513	0.31
DGP 21.17	251.945	0.113	251.963	0.480	0.42	0.56	39.56	0.63	3736	0.0398	0.05	0.2816	0.22	0.0513	0.20
DGP 21.18	251.896	0.230	251.998	1.429	0.75	0.61	11.49	0.61	1119	0.0398	0.09	0.2817	0.64	0.0513	0.60
DGP 21.20	251.976	0.074	252.081	0.523	0.77	0.57	29.35	0.59	2997	0.0398	0.03	0.2818	0.23	0.0513	0.23
DGP 21.21	251.940	0.172	252.109	1.486	1.02	0.62	10.01	0.58	1028	0.0398	0.07	0.2818	0.67	0.0513	0.65
Dongpan-17															
DGP 17.1	252.018	0.091	252.079	0.325	0.61	0.43	64.38	0.69	5792	0.0399	0.04	0.2818	0.15	0.0513	0.13
DGP 17.2	252.896	0.108	252.753	0.473	-0.23	0.50	36.24	0.51	4303	0.0400	0.04	0.2826	0.21	0.0513	0.19
DGP 17.3	251.899	0.096	252.006	0.514	0.80	0.44	31.56	0.60	3230	0.0398	0.04	0.2817	0.23	0.0513	0.22
DGP 17.4	251.871	0.120	252.189	0.623	1.64	0.44	25.52	0.56	2837	0.0398	0.05	0.2819	0.28	0.0514	0.26
DGP 17.5	251.990	0.131	251.620	0.505	-1.16	0.46	35.56	0.52	4195	0.0398	0.05	0.2812	0.23	0.0512	0.20
DGP 17.6	252.001	0.063	252.195	0.323	1.15	0.41	48.16	0.53	5661	0.0399	0.03	0.2819	0.14	0.0513	0.13
DGP 17.7	251.933	0.120	252.166	0.897	1.30	0.51	16.80	0.58	1773	0.0398	0.05	0.2819	0.40	0.0513	0.39
DGP 17.8	251.927	0.193	252.158	2.208	1.31	0.33	15.56	1.53	663	0.0398	0.08	0.2819	0.99	0.0513	0.99
DGP 17.9	251.929	0.101	252.328	0.493	1.96	0.41	30.66	0.54	3543	0.0398	0.04	0.2821	0.22	0.0514	0.21
DGP 17.10	252.003	0.210	252.585	0.637	2.67	0.41	20.82	0.51	2568	0.0399	0.08	0.2824	0.28	0.0514	0.27
DGP 17.11	251.938	0.118	252.124	0.330	1.13	0.36	42.18	0.49	5401	0.0398	0.05	0.2819	0.15	0.0513	0.13
DGP 17.12	251.866	0.158	251.890	0.478	0.46	0.45	29.58	0.52	3536	0.0398	0.06	0.2816	0.21	0.0513	0.20
Dongpan-16															
DGP 16.1	252.074	0.177	250.746	0.953	-5.34	0.37	20.74	0.73	1809	0.0399	0.07	0.2801	0.43	0.0510	0.41
DGP 16.3	252.008	0.113	251.757	1.091	-0.67	0.49	17.10	0.76	1388	0.0399	0.05	0.2814	0.49	0.0512	0.48
DGP 16.4	251.959	0.074	252.180	0.469	1.28	0.22	27.97	0.53	3469	0.0398	0.03	0.2819	0.21	0.0513	0.20

772

773 **Tab. B1. continued.**

Fraction and sample	Dates (Ma)					Composition				Isotopic Ratios					
	206Pb/238U *a°°	±2σ (absolute)	207Pb/235U *a	±2σ (absolute)	Disc. (%) *b	Th/U *c	Pb (pg) *d	Pbc (pg) *e	206Pb/204Pb *f	206Pb/238U *g	±2σ (%)	207Pb/235U *g	±2σ (%)	207Pb/206Pb *g	±2σ (%)
DGP 16.5	252.018	0.149	251.175	1.164	-3.19	0.45	16.74	0.71	1456	0.0399	0.06	0.2807	0.52	0.0511	0.50
DGP 16.7	251.959	0.134	252.150	0.937	1.17	0.19	14.52	0.58	1673	0.0398	0.05	0.2819	0.42	0.0513	0.41
DGP 16.8	251.926	0.102	252.727	0.668	3.54	0.24	20.15	0.51	2607	0.0398	0.04	0.2826	0.30	0.0515	0.29
DGP 16.9	251.471	0.160	251.540	0.778	0.67	0.27	21.37	0.66	2095	0.0398	0.06	0.2811	0.35	0.0513	0.33
DGP 16.10	252.030	0.168	252.627	1.555	2.73	0.39	12.30	0.75	1041	0.0399	0.07	0.2825	0.70	0.0514	0.68
DGP 16.12	252.023	0.107	251.841	0.508	-0.35	0.26	24.27	0.49	3228	0.0399	0.04	0.2815	0.23	0.0512	0.21
DGP 16.13	251.897	0.158	252.166	0.703	1.47	0.27	18.84	0.51	2396	0.0398	0.06	0.2819	0.31	0.0514	0.30
Dongpan-13															
DGP 13.1	252.103	0.104	252.698	0.859	2.73	0.36	22.62	0.83	1727	0.0399	0.04	0.2826	0.38	0.0514	0.38
DGP 13.2	252.079	0.069	252.151	0.246	0.66	0.41	60.43	0.41	9091	0.0399	0.03	0.2819	0.11	0.0513	0.09
DGP 13.3	252.174	0.104	252.415	0.877	1.33	0.43	14.18	0.51	1738	0.0399	0.04	0.2822	0.39	0.0513	0.38
DGP 13.4	252.118	0.153	252.094	0.691	0.27	0.42	20.60	0.55	2331	0.0399	0.06	0.2818	0.31	0.0513	0.29
DGP 13.5	252.086	0.115	252.042	0.369	0.21	0.29	31.43	0.37	5516	0.0399	0.05	0.2817	0.17	0.0513	0.12
DGP 13.7	252.067	0.081	252.029	0.518	0.21	0.46	23.69	0.47	3095	0.0399	0.03	0.2817	0.23	0.0513	0.22
DGP 13.8	252.155	0.123	251.914	0.779	-0.63	0.45	18.88	0.57	2056	0.0399	0.05	0.2816	0.35	0.0512	0.34
Dongpan-12															
DGP 12.1	252.146	0.107	252.081	0.699	0.10	0.45	16.28	0.43	2346	0.0399	0.04	0.2818	0.31	0.0513	0.30
DGP 12.4	252.131	0.112	252.317	0.855	1.10	0.55	13.00	0.42	1864	0.0399	0.05	0.2821	0.38	0.0513	0.37
DGP 12.5	252.065	0.093	251.950	0.506	-0.09	0.35	25.11	0.44	3646	0.0399	0.04	0.2816	0.23	0.0513	0.21
DGP 12.6	252.032	0.112	252.101	0.777	0.63	0.54	13.84	0.41	2033	0.0399	0.05	0.2818	0.35	0.0513	0.33
DGP 12.7	252.159	0.090	252.536	0.804	1.86	0.50	12.34	0.39	1925	0.0399	0.04	0.2824	0.36	0.0514	0.35
DGP 12.8	252.102	0.094	252.185	0.586	0.66	0.69	19.34	0.40	2786	0.0399	0.04	0.2819	0.26	0.0513	0.25
DGP 12.9	252.224	0.148	251.873	0.892	-1.11	0.63	9.37	0.25	2253	0.0399	0.06	0.2815	0.40	0.0512	0.37
DGP 12.10	252.142	0.075	252.212	0.485	0.66	0.33	17.96	0.34	3371	0.0399	0.03	0.2820	0.22	0.0513	0.21
Dongpan-11															
DGP 11.1	252.458	0.208	252.299	1.063	-0.26	0.31	10.86	0.43	1626	0.0399	0.08	0.2821	0.48	0.0513	0.45
DGP 11.3	251.912	0.224	251.970	0.943	0.62	0.30	11.81	0.40	1889	0.0398	0.09	0.2817	0.42	0.0513	0.40
DGP 11.4	251.661	0.263	251.688	0.952	0.47	0.48	12.56	0.39	1957	0.0398	0.11	0.2814	0.43	0.0513	0.39
DGP 11.5	252.924	0.352	251.794	3.262	-4.43	0.43	2.37	0.31	498	0.0400	0.14	0.2814	1.46	0.0511	1.44
DGP 11.6	251.861	0.202	251.725	1.029	-0.17	0.29	11.14	0.43	1692	0.0398	0.08	0.2813	0.46	0.0513	0.45
DGP 11.7	252.881	0.571	252.626	6.500	-0.68	0.48	1.78	0.46	253	0.0400	0.23	0.2825	2.91	0.0513	2.88
DGP 11.8	252.039	0.210	251.722	1.798	-0.91	0.27	5.43	0.36	982	0.0399	0.09	0.2813	0.81	0.0512	0.78
DGP 11.10	251.884	0.274	252.117	2.953	1.32	0.31	5.30	0.66	528	0.0398	0.11	0.2818	1.32	0.0513	1.31
DGP 11.11	252.635	0.218	252.640	2.345	0.39	0.44	5.50	0.54	644	0.0400	0.09	0.2825	1.05	0.0513	1.04
DGP 11.12	252.155	0.257	252.014	2.254	-0.21	0.41	6.27	0.55	723	0.0399	0.10	0.2817	1.01	0.0513	0.99
DGP 11.14	252.580	0.316	252.776	3.295	1.16	0.35	4.95	0.59	545	0.0399	0.13	0.2827	1.47	0.0513	1.44
Dongpan-10															
DGP 10.1	252.088	0.150	251.900	0.762	-0.40	0.40	19.51	0.51	2402	0.0399	0.06	0.2816	0.34	0.0512	0.32
DGP 10.4	252.126	0.317	252.075	2.243	0.16	0.44	6.97	0.62	708	0.0399	0.13	0.2818	1.00	0.0513	0.99
DGP 10.5	252.142	0.121	252.084	0.815	0.14	0.38	11.87	0.38	1965	0.0399	0.05	0.2818	0.37	0.0513	0.35
DGP 10.6	252.770	0.183	252.896	1.847	0.87	0.45	4.97	0.39	807	0.0400	0.07	0.2828	0.82	0.0513	0.82

774

775 **Tab. B1. continued.**

Fraction and sample	Dates (Ma) 206Pb/238U *a°°	±2σ (absolute)	207Pb/235U *a	±2σ (absolute)	Disc. (%) *b	Composition Th/U *c	Pb (pg) *d	Pbc (pg) *e	206Pb/204Pb *f	Isotopic Ratios 206Pb/238U *g	±2σ (%)	207Pb/235U *g	±2σ (%)	207Pb/206Pb *g	±2σ (%)
DGP 10.7	252.147	0.091	252.590	0.708	2.13	0.40	14.72	0.42	2199	0.0399	0.04	0.2824	0.32	0.0514	0.31
DGP 10.8	252.769	0.204	252.740	1.368	0.25	0.42	8.93	0.48	1180	0.0400	0.08	0.2826	0.61	0.0513	0.59
DGP 10.9	252.254	0.242	252.244	1.725	0.33	0.39	6.12	0.43	904	0.0399	0.10	0.2820	0.77	0.0513	0.76
DGP 10.11	252.366	0.181	252.211	1.025	-0.26	0.43	10.91	0.41	1669	0.0399	0.07	0.2820	0.46	0.0513	0.44
DGP 10.12	252.201	0.159	252.379	0.861	1.06	0.55	12.49	0.42	1802	0.0399	0.06	0.2822	0.39	0.0513	0.37
DGP 10.13	252.826	0.424	252.481	2.031	-1.06	0.47	5.98	0.40	933	0.0400	0.17	0.2823	0.91	0.0512	0.86
Penglaitan-22															
PEN 22.2	251.909	0.073	251.819	0.444	0.00	0.44	36.92	0.50	4573	0.0398	0.03	0.2815	0.20	0.0513	0.20
PEN 22.3	251.405	0.174	251.671	0.358	1.44	0.43	46.73	0.53	5494	0.0398	0.07	0.2813	0.16	0.0513	0.13
PEN 22.4	251.895	0.080	252.071	0.360	1.09	0.35	38.18	0.46	5207	0.0398	0.03	0.2818	0.16	0.0513	0.14
PEN 22.6	251.910	0.055	252.004	0.366	0.77	0.28	29.59	0.46	4155	0.0398	0.02	0.2817	0.16	0.0513	0.16
PEN 22.7	251.964	0.237	251.667	1.108	-0.86	0.48	13.37	0.51	1614	0.0398	0.10	0.2813	0.50	0.0512	0.46
PEN 22.8	252.166	0.123	252.092	1.220	0.10	0.17	8.09	0.44	1248	0.0399	0.05	0.2818	0.55	0.0513	0.54
PEN 22.9	252.166	0.123	252.210	1.229	0.53	0.55	13.03	0.63	1252	0.0399	0.05	0.2820	0.55	0.0513	0.54
PEN 22.10	251.939	0.156	252.332	1.313	1.93	0.51	14.37	0.72	1229	0.0398	0.06	0.2821	0.59	0.0514	0.57
PEN 22.11	251.891	0.082	251.861	0.715	0.25	0.40	20.94	0.62	2139	0.0398	0.03	0.2815	0.32	0.0513	0.31
PEN 22.12	251.913	0.157	251.527	0.818	-1.19	0.18	6.21	0.14	2866	0.0398	0.06	0.2811	0.37	0.0512	0.33
PEN 22.13	251.923	0.205	251.163	1.490	-2.82	0.35	4.24	0.14	1895	0.0398	0.08	0.2806	0.67	0.0511	0.63
Penglaitan-28															
PEN 28.1	252.511	0.198	251.772	1.001	-2.75	0.60	18.86	0.67	1668	0.0399	0.08	0.2814	0.45	0.0511	0.43
PEN 28.2	252.078	0.083	252.151	0.760	0.64	0.59	22.29	0.64	2081	0.0399	0.03	0.2819	0.34	0.0513	0.34
PEN 28.3	252.057	0.106	252.080	0.597	0.43	0.65	25.69	0.52	2916	0.0399	0.04	0.2818	0.27	0.0513	0.25
PEN 28.4	252.096	0.086	252.096	0.536	0.35	0.57	25.37	0.52	2913	0.0399	0.03	0.2818	0.24	0.0513	0.23
PEN 28.5	252.364	0.156	252.603	1.227	1.25	0.96	10.94	0.47	1277	0.0399	0.06	0.2825	0.55	0.0513	0.54
PEN 28.6	252.045	0.119	251.936	1.366	-0.10	0.58	14.53	0.82	1074	0.0399	0.05	0.2816	0.61	0.0513	0.62
PEN 28.7	251.989	0.144	252.023	0.676	0.49	0.56	28.93	0.62	2784	0.0399	0.06	0.2817	0.30	0.0513	0.28
PEN 28.8	252.174	0.367	251.129	2.321	-4.10	0.59	4.11	0.37	680	0.0399	0.15	0.2806	1.04	0.0511	1.02
PEN 28.9	252.430	0.286	252.213	1.763	-0.56	0.69	6.03	0.40	898	0.0399	0.12	0.2820	0.79	0.0512	0.77
PEN 28.10	252.413	0.245	252.919	2.130	2.32	0.80	6.63	0.53	724	0.0399	0.10	0.2829	0.95	0.0514	0.94
PEN 28.11	251.994	0.167	252.168	0.996	1.04	0.63	10.75	0.39	1621	0.0399	0.07	0.2819	0.45	0.0513	0.43
PEN 28.12	252.403	0.284	252.540	1.982	0.89	0.61	6.77	0.52	789	0.0399	0.11	0.2824	0.89	0.0513	0.87
PEN 28.13	253.090	0.375	252.838	2.764	-0.69	0.64	3.87	0.42	559	0.0400	0.15	0.2828	1.24	0.0513	1.22
Penglaitan-70															
PEN 70.1	253.371	0.165	253.002	1.461	-1.21	0.87	16.24	0.87	1054	0.0401	0.07	0.2830	0.65	0.0512	0.64
PEN 70.2	252.917	0.220	252.968	0.711	0.54	0.61	36.74	0.98	2233	0.0400	0.09	0.2829	0.32	0.0513	0.30
PEN 70.3	252.778	0.270	252.955	1.111	1.04	0.64	17.72	0.65	1618	0.0400	0.11	0.2829	0.50	0.0513	0.47
PEN 70.4	252.137	0.200	252.078	0.967	0.10	0.62	16.95	0.57	1769	0.0399	0.08	0.2818	0.43	0.0513	0.41
PEN 70.6	252.519	0.125	252.436	0.510	0.01	0.57	34.71	0.65	3223	0.0399	0.05	0.2822	0.23	0.0513	0.22
PEN 70.7	253.079	0.283	253.701	1.493	2.70	1.22	20.94	1.04	1039	0.0400	0.11	0.2838	0.67	0.0515	0.64
PEN 70.8	253.309	0.231	253.620	1.294	1.55	0.81	13.88	0.67	1180	0.0401	0.09	0.2837	0.58	0.0514	0.57
PEN 70.9	252.156	0.147	252.327	0.404	1.03	0.64	52.32	0.56	5516	0.0399	0.06	0.2821	0.18	0.0513	0.16

776

777 **Tab. B1. continued.**

Fraction and sample	Dates (Ma)					Composition				Isotopic Ratios					
	206Pb/238U *a°°	±2σ (absolute)	207Pb/235U *a	±2σ (absolute)	Disc. (%) *b	Th/U *c	Pb (pg) *d	Pbc (pg) *e	206Pb/204Pb *f	206Pb/238U *g	±2σ (%)	207Pb/235U *g	±2σ (%)	207Pb/206Pb *g	±2σ (%)
PEN 70.10	253.036	0.339	253.063	0.777	0.45	0.59	19.61	0.52	2261	0.0400	0.14	0.2830	0.35	0.0513	0.31
PEN 70.11	251.994	0.169	252.052	0.446	0.56	0.69	51.50	0.66	4508	0.0399	0.07	0.2818	0.20	0.0513	0.17
PEN 70.12	252.153	0.230	252.159	1.201	0.37	0.60	13.80	0.51	1616	0.0399	0.09	0.2819	0.54	0.0513	0.51
PEN 70.13	253.341	0.128	253.340	1.121	0.31	0.77	11.91	0.51	1345	0.0401	0.05	0.2834	0.50	0.0513	0.49
PEN 70.14	253.136	0.228	253.163	1.951	0.43	0.70	13.35	0.93	846	0.0400	0.09	0.2832	0.87	0.0513	0.86
PEN 70.16	252.515	0.105	252.243	0.348	-0.72	0.27	16.42	0.16	6680	0.0399	0.04	0.2820	0.16	0.0512	0.13
PEN 70.17	252.215	0.350	251.974	0.528	-0.65	0.61	15.81	0.17	5572	0.0399	0.14	0.2817	0.24	0.0512	0.17
PEN 70.19	252.166	0.127	252.256	0.253	0.67	0.86	43.54	0.28	8650	0.0399	0.05	0.2820	0.11	0.0513	0.09
PEN 70.20	252.676	0.258	252.493	0.385	-0.39	0.50	20.85	0.16	7842	0.0400	0.10	0.2823	0.17	0.0513	0.12
PEN 70.22	252.062	0.274	251.239	0.831	-3.11	0.55	19.83	0.32	3682	0.0399	0.11	0.2807	0.37	0.0511	0.27
Penglaitan-6															
PEN 6.1	252.889	0.295	254.066	3.159	4.87	0.59	9.05	1.14	486	0.0400	0.12	0.2843	1.41	0.0516	1.39
PEN 6.2	253.231	0.184	253.518	1.674	1.48	0.58	6.96	0.45	926	0.0401	0.07	0.2836	0.75	0.0514	0.73
PEN 6.3	253.745	0.241	253.643	2.159	-0.09	0.67	6.16	0.49	740	0.0401	0.10	0.2838	0.96	0.0513	0.94
PEN 6.4	252.679	0.102	253.035	0.688	1.76	0.59	19.60	0.48	2435	0.0400	0.04	0.2830	0.31	0.0514	0.30
PEN 6.5	252.123	0.099	252.325	0.612	1.16	0.56	26.32	0.52	3029	0.0399	0.04	0.2821	0.27	0.0513	0.25
PEN 6.7	252.754	0.240	254.068	2.670	5.35	0.70	7.16	0.74	575	0.0400	0.10	0.2843	1.19	0.0516	1.18
PEN 6.10	253.199	0.319	254.546	2.200	5.41	1.00	5.97	0.45	722	0.0400	0.13	0.2849	0.98	0.0516	0.96
PEN 6.12	252.793	0.229	252.635	1.453	-0.30	0.59	8.32	0.46	1080	0.0400	0.09	0.2825	0.65	0.0513	0.63
PEN 6.13	252.728	0.187	253.169	1.293	2.09	0.62	9.76	0.49	1193	0.0400	0.08	0.2832	0.58	0.0514	0.57
PEN 6.14	252.550	0.205	252.547	1.986	0.33	0.57	6.68	0.51	791	0.0399	0.08	0.2824	0.89	0.0513	0.87
PEN 6.15	252.161	0.237	251.253	1.230	-3.51	0.68	6.78	0.19	2134	0.0399	0.10	0.2808	0.55	0.0511	0.52
PEN 6.16	252.567	0.183	252.405	1.351	-0.36	0.93	5.33	0.22	1358	0.0399	0.07	0.2822	0.60	0.0513	0.57
PEN 6.17	252.862	0.144	252.540	1.143	-0.97	0.51	6.78	0.28	1464	0.0400	0.06	0.2824	0.51	0.0512	0.49
PEN 6.18	252.172	0.191	249.752	0.886	-10.60	0.41	8.95	0.19	2959	0.0399	0.08	0.2789	0.40	0.0507	0.31
PEN 6.19	252.581	0.145	252.136	0.535	-1.50	0.63	12.68	0.20	3724	0.0399	0.06	0.2819	0.24	0.0512	0.23

a Isotopic dates calculated using the decay constants λ238 = 1.55125E-10 and λ235 = 9.8485E-10 (Jaffey et al., 1971).

b % discordance = 100 - (100 * (206Pb/238U date) / (207Pb/206Pb date)).

c Th contents calculated from radiogenic 208Pb and the 207Pb/206Pb date of the sample, assuming concordance between U-Th and Pb systems.

d Total mass of radiogenic Pb.

e Total mass of common Pb.

f Measured ratio corrected for fractionation and spike contribution only.

g Measured ratio corrected for fractionation, tracer and blank.

°° Corrected for initial Th/U disequilibrium using radiogenic 208Pb and Th/U_magma = 3.00.

* Samples marked in red are from a previous study (Baresel et al., in press).

779 Baresel, B., D'Abzac, F.X., Bucher, H., and Schaltegger, U.: High-precision time-space correlation through coupled apatite
780   and zircon tephrochronology: an example from the Permian-Triassic boundary in South China. Geology,
781   doi:10.1130/G38181.1, *in press*.

782 Bowring, J.F., McLean, N.M., and Bowring, S.A.: Engineering cyber infrastructure for U-Pb geochronology: tripoli and U-
783   Pb_Redux. Geochem. Geophy. Geosy., 12, Q0AA19, doi:10.1029/2010GC003479, 2011.

784 Condon, D.J., Schoene, B., McLean, N.M., Bowring, S.A., and Parrish, R.R.: Metrology and traceability of U-Pb isotope
785   dilution geochronology (EARTHTIME Tracer Calibration Part I). Geochim. Cosmochim. Ac., 164, 464–480,
786   doi:10.1016/j.gca.2015.05.026, 2015.

787 Gerstenberger, H., and Haase, G.: A highly effective emitter substance for mass spectrometric Pb isotope ratio
788   determination. Chem. Geol., 136, 309–312, doi:10.1016/S0009-2541(96)00033-2, 1997.

789 Hiess, J., Condon, D.J., McLean, N.M., and Noble, S.R.: ^{238}U/^{235}U Systematics in terrestrial uranium-bearing minerals.
790   Science, 335, 1610–1614, doi:10.1126/science.1215507, 2012.

791 Jaffey, A.H., Flynn, K.F., Glendenin, L.E., Bentley, W.C., and Essling, A.M.: Precision measurements of half-lives and
792   specific activities of ^{235}U and ^{238}U. Phys. Rev. C, 4, 1889–1906, doi:10.1103/physrevc.4.1889, 1971.

793 Krogh, T.E.: A low contamination method for hydrothermal decomposition of zircon and extraction of U and Pb for isotopic
794   age determination. Geochim. Cosmochim. Ac., 37, 485–494, doi:10.1016/0016-7037(73)90213-5, 1973.

795 Mattinson, J.M.: Zircon U-Pb chemical abrasion ("CA-TIMS") method: combined annealing and multi-step partial
796   dissolution analysis for improved precision and accuracy of zircon ages. Chem. Geol., 220, 47–66,
797   doi:10.1016/j.chemgeo.2005.03.011, 2005.

798 McLean, N.M., Bowring, J.F., and Bowring, S.A.: An algorithm for U-Pb isotope dilution data reduction and uncertainty
799   propagation. Geochem. Geophy. Geosy., 12, Q0AA18, doi:10.1029/2010GC003478, 2011.

800 Ovtcharova, M., Goudemand, N., Hammer, O., Guodun, K., Cordey, F., Galfetti, T., Schaltegger, U., and Bucher, H.:
801   Developing a strategy for accurate definition of a geological boundary through radio-isotopic and biochronological
802   dating: The Early–Middle Triassic boundary (South China). Earth-Sci. Rev., 146, 65–76,
803   doi:10.1016/j.earscirev.2015.03.006, 2015.

804

805

806

807

808

Appendix C: Dongpan radiolarians

Feng et al. (2007) suggested that radiolarian faunas underwent two successive extinction phases in Dongpan. Their first radiolarian crisis (FRC) occurs in bed 6 and their second radiolarian crisis (SRC) in bed 8 (see Appendix D). Hence, these authors proposed that the decline of radiolarians preceded a late Permian mass extinction (LPME; see Appendix D) placed in bed 9 on the basis of impoverished brachiopod, foraminifera and ostracod faunas (He et al., 2007; Yin et al., 2007) and of a negative excursion of the $\delta^{13}C_{org}$ record (Zhang et al., 2006). Subsequently, Feng and Algeo (2014) published a new radiolarian diversity curve showing the initiation of a protracted decline ("preliminary extinction": PE) starting in the middle part of bed 5. The second radiolarian crisis as initially recognized by Feng et al. (2007) is no longer visible in this progressive diversity reduction at the species level.

As radiolarians are well known to be highly sensitive to selective preservation bias, the comparison of this apparent diversity change with excess SiO_2 brings further insights. Shen et al. (2012) plotted excess SiO_2 along the Dongpan section but it is unclear how much biogenic or volcanogenic silica respectively contributed to these values. Above bed 9, Shen et al. (2012) also indicate absence of kaolinite in the clay fraction, suggesting that a lack of volcaniclastic input did contribute to the low levels of excess SiO_2. This drop of kaolinite and excess SiO_2 corresponds to the LPME of Feng et al. (2007) and to a lesser degree to the "main extinction" (ME) of Feng and Algeo (2014), which they placed in bed 8. The coincidence between the drop of excess SiO_2 and the LPME and/or the ME does not enable distinguishing a real extinction event of the radiolarians from a selective preservation bias.

Feng and Algeo (2014) interpreted the onset of the radiolarian decline in bed 5 as being morphologically selective, with long-spined species of the orders *Spumellaria* and *Entactinaria* preferentially going extinct relative to short-spined species. However, such a statement requires precise investigation of the effects of diagenesis on a bed by bed basis, as post-depositional dissolution can be extremely heterogeneous and guided by minor differences of available amount of SiO_2 in each bed. The model proposed by Feng and Algeo (2014) for the evolution of radiolarian-bearing rocks calls upon changes of oceanic redox conditions during the Permo-Triassic transition. This model is based on the assumption that Permian radiolarians can be divided into three paleoecological assemblages based on proportions between four orders (*Entactinaria*, *Spumellaria*, *Latentifistularia* and *Albaillellaria*), each restricted to shallow-, intermediate-, and deep-water environments. Dongpan was one of the main examples used to support the claim that radiolarians were differentially affected around the PTB events by an expansion of the oxygen minimum zone (OMZ). According to their scenario, deep-water taxa declined earlier than shallow-water taxa as a result of an expansion of the OMZ. This ecological model of radiolarian stratification with partial mutual taxonomic exclusion is only loosely supported by well-constrained Late Permian data worldwide and is not supported when compared to the present-day planktonic mixing and diversity at any depth. Present-day studies on the silica cycle (e.g., Tréguer and De La Rocha, 2013) show that biosiliceous deposits are strongly affected by post-depositional dissolution at the water-sediment interface and during diagenesis. Last but not least, evidences supporting a rise of the OMZ in Dongpan are lacking.

842
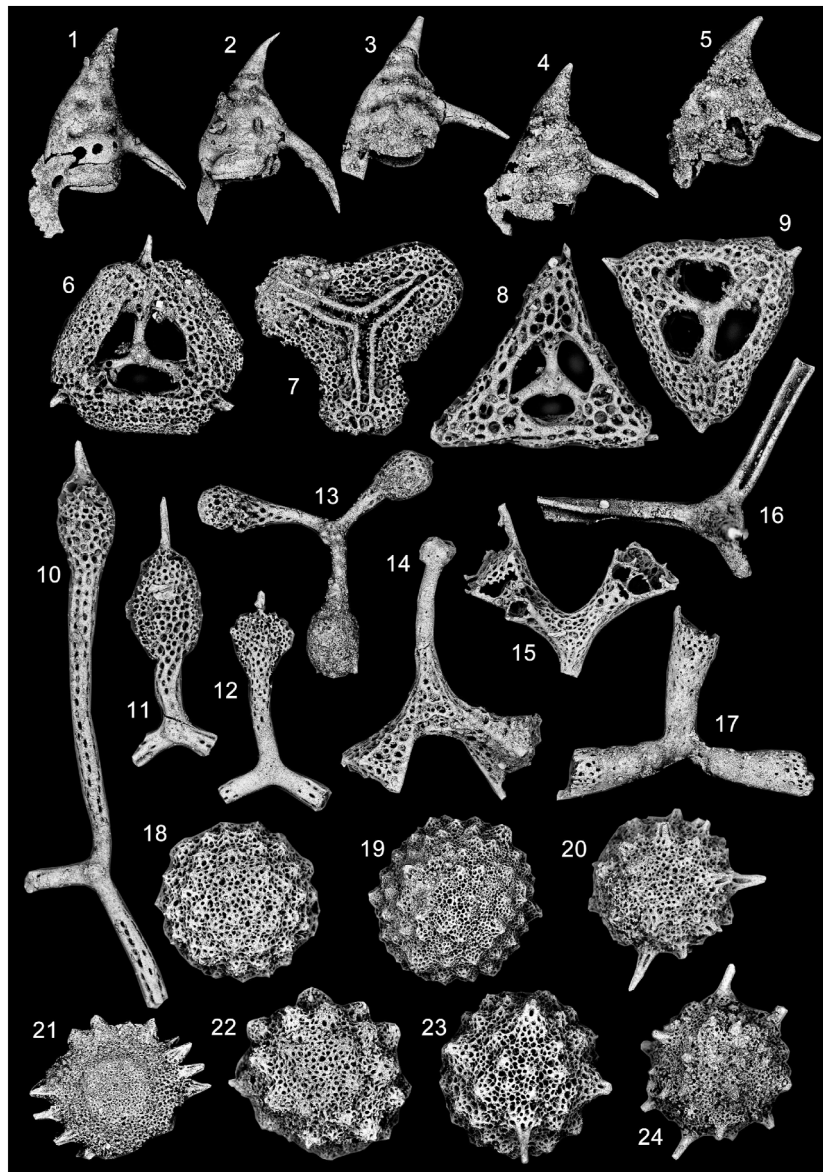
Fig. C1. Plate of Dongpan radiolarians ordered by taxon, sample, database number, and maximum dimension. 1) Albaillella yaoi Kuwahara, DGP-2, n°20, 200 μm. 2) Albaillella triangularis Ishiga, Kito & Imoto, DGP-2, n° 21, 210 μm. 3) Albaillella triangularis Ishiga, Kito & Imoto, DGP-1, n°06, 170 μm. 4) Albaillella triangularis Ishiga, Kito & Imoto, DGP-1, n° 11, 190 μm. 5) Albaillella levis Ishiga, Kito & Imoto, DGP-1, n°07, 190 μm. 6) Foremanhelena circula Shang, Caridroit & Wang, DGP-2, n°02, 260 μm. 7) Triplanospongos musashiensis Sashida & Tonishi, DGP-2, n°03, 260 μm. 8) Foremanhelena robusta Feng, DGP-2, n°05, 220 μm. 9) Foremanhelena robusta Feng, DGP-2, n°12, 230 μm. 10) Ishigaum tristylum Feng, DGP-2, n°11, 700 μm. 11) Ishigaum fusinum Feng, DGP-2, n°10, 400 μm. 12) Ishigaum sp., DGP-2, n°13, 270 μm. 13) Cauletella delicata Caridroit & Shang, DGP-5, n°03, 260 μm. 14) Cauletella paradoxa Shang, Caridroit & Wang, DGP-2, n°07, 400 μm. 15) Cauletella paradoxa Shang, Caridroit & Wang, DGP-2, n°09, 300 μm. 16) Nazarovella gracilis De Wever & Caridroit, DGP-5, n°04, 350 μm. 17) Cauletella manica De Wever & Caridroit, DGP-2, n°14, 210 μm. 18) Hegleria mammilla Sheng & Wang, DGP-2, n°30, 290 μm. 19) Hegleria sp. aff. mammilla Sheng & Wang, DGP-5, n°15, 300 μm. 20) Paracopycintra ziyunensis Feng & Gu, DGP-5, n°18, 270 μm. 21) Copicyntroides sp., DGP-5, n°01, 310 μm. 22) Paracopycintra sp., DGP-5, n°12, 300 μm. 23) Paracopycintra akikawaensis Sashida & Tonishi, DGP-2, n°36, 280 μm. 24) Paracopycintra akikawaensis Sashida & Tonishi, DGP-2, n°33, 300 μm.

856 Feng, Q.L., and Algeo, T.J.: Evolution of oceanic redox conditions during the Permo-Triassic transition: Evidence from
857   deepwater radiolarian facies. Earth-Sci. Rev., 137, 34–51, doi:10.1016/j.earscirev.2013.12.003, 2014.

858 Feng, Q.L., He, W.H., Gu, S.Z., Meng, Y.Y., Jin, Y.X., and Zhang, F.: Radiolarian evolution during the latest Permian in
859   South China. Global Planet. Change, 55, 177–192, doi:10.1016/j.gloplacha.2006.06.012, 2007.

860 He, W.H., Shi, G.R., Feng, Q.L., Campi, M.J., Gu, S.Z., Bu, J.J., Peng, Y.Q., and Meng, Y.Y.: Brachiopod miniaturization
861   and its possible causes during the Permian-Triassic crisis in deep water environments, South China. Palaeogeogr.
862   Palaeocl., 252, 145–163, doi:10.1016/j.palaeo.2006.11.040, 2007.

863 Shen, J., Algeo, T.J., Zhou, L., Feng, Q., Yu, J., and Ellwood, B.: Volcanic perturbations of the marine environment in South
864   China preceding the latest Permian mass extinction and their biotic effects. Geobiology, 10, 82–103, 2012.

865 Tréguer, P.J., and De La Rocha, C.L.: The world ocean silica cycle. Annu. Rev. Mar. Sci., 5, 477–501, doi:10.1146/annurev-
866   marine-121211-172346, 2013.

867 Yin, H.F., Feng, Q.L., Lai, X.L., Baud, A., and Tong, J.N.: The protracted Permo-Triassic crisis and multi-episode extinction
868   around the Permian-Triassic boundary. Global Planet. Change, 55, 1–20, doi:10.1016/j.gloplacha.2006.06.005, 2007.

869 Zhang, F., Feng, Q.I., Meng, Y.Y., He, W.H., and Gu, S.Z.: Stratigraphy of organic carbon isotope and associated events
870   across the Permian and Triassic boundary in the Dongpan deepwater section in Liuqiao area, Guangxi, South China.
871   Geoscience, 20, 1, 42–48, 2006.

872
873
874
875
876
877
878

879 **Appendix D: Penglaitan conodonts**
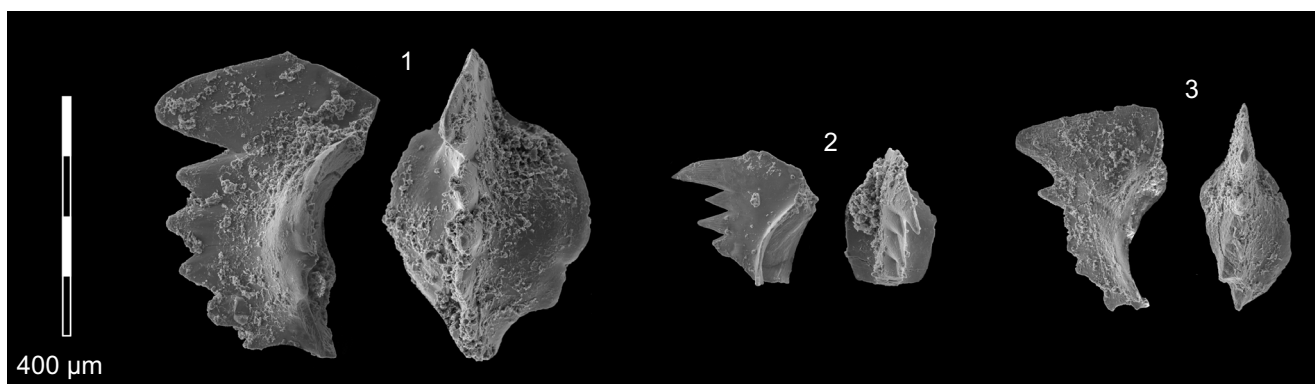
880

881 **Fig. D1. Plate of Penglaitan conodonts ordered by taxon, sample number and conodont Unitary Associations zones after Brosse et**
882 **al. (2016). 1) *Hindeodus inflatus* Nicoll, Metcalfe and Cheng-Yuan, PEN-23, UAZ3-UAZ5 (Griesbachian). The distal denticle is**
883 **broader and slightly higher than the five posterior denticles. The denticles are evenly appressed along the carina, which is in**
884 **contrast with holotype of *H. inflatus* Nicoll, Metcalfe and Cheng-Yuan. The height of the denticles decreases posteriorly,**
885 **comparable to that of *H. postparvus* Kozur morphotype 1. In upper view, the carina is laterally compressed and rises directly from**
886 **the expanded cup. The cup is symmetrical and much expanded. It opens from the distal denticle to the posterior end of the**
887 **element. 2) *Hindeodus parvus* Kozur and Pjatakova (juvenile), PEN-23, UAZ3-UAZ5 (Griesbachian). The distal denticle is very**
888 **high compared to the adjacent denticles. Only three denticles are following in this juvenile element. The blade rises from the round**
889 **and symmetrical cup. 3) *Hindeodus ?praeparvus* Kozur, PEN-24. The distal denticle is broad and tall. Although most of the**
890 **denticles of the carina are broken, the height of the carina seems to progressively decrease posteriorly. From his outline, this**
891 **element resembles *H. typicalis* Sweet, with a progressive posterior inclination of the carina. The widely oppressed denticles seem to**
892 **indicate a closer relation to *H. praeparvus* Kozur.**

893

894 Brosse, M., Bucher, H., and Goudemand, N.: Quantitative biochronology of the Permian-Triassic boundary in South China

895   based on conodont Unitary Associations. Earth-Sci. Rev., 155, 153–171, doi:10.1016/j.earscirev.2016.02.003, 2016.